2017

Nitroxide-Based Macromolecular Contrast Agents with Unprecedented Transverse Relaxivity and Stability for Magnetic Resonance Imaging of Tumors

Hung V.T. Nguyen

Qixian Chen

Joseph T. Paletta

Peter Harvey

Yivan Jiang

See next page for additional authors

Authors

Hung V.T. Nguyen, Qixian Chen, Joseph T. Paletta, Peter Harvey, Yivan Jiang, Hui Zhang, Michael Boska, M. Francesca Ottaviani, Alan Jasanoff, Andrzej Rajca, and Jeremiah A. Johnson

ACS central science

Research Article

http://pubs.acs.org/journal/acscii

Nitroxide-Based Macromolecular Contrast Agents with Unprecedented Transverse Relaxivity and Stability for Magnetic Resonance Imaging of Tumors

Hung V.-T. Nguyen,[†] Qixian Chen,[†] Joseph T. Paletta,[‡] Peter Harvey,[∥] Yivan Jiang,[†] Hui Zhang,[‡] Michael D. Boska,[§,¶] M. Francesca Ottaviani,[▽] Alan Jasanoff,[∥,⊥,#] Andrzej Rajca,[‡] and Jeremiah A. Johnson*[,†]

[†]Department of Chemistry, [∥]Department of Biological Engineering, [⊥]Department of Brain and Cognitive Sciences, and [#]Department of Nuclear Science and Engineering, Massachusetts Institute of Technology, 77 Massachusetts Avenue, Cambridge, Massachusetts 02139, United States

[§]Department of Radiology, University of Nebraska Medical Center, Omaha, Nebraska 68198, United States

[▽]Department of Pure and Applied Sciences, University of Urbino, Urbino 61029, Italy

[‡]Department of Chemistry, University of Nebraska, Lincoln, Nebraska 68588, United States

Supporting Information

ABSTRACT: Metal-free magnetic resonance imaging (MRI) agents could overcome the established toxicity associated with metal-based agents in some patient populations and enable new modes of functional MRI *in vivo*. Herein, we report nitroxide-functionalized brush-arm star polymer organic radical contrast agents (BASP-ORCAs) that overcome the low contrast and poor *in vivo* stability associated with nitroxide-based MRI contrast agents. As a consequence of their unique nano-architectures, BASP-ORCAs possess per-nitroxide transverse relaxivities up to ∼44-fold greater than common nitroxides, exceptional stability in highly reducing environments, and low toxicity. These features combine to provide for accumulation of a sufficient concentration of BASP-ORCA in murine subcutaneous tumors up to 20 h following systemic administration such that MRI contrast on par with metal-based agents is observed. BASP-ORCAs are, to our knowledge, the first nitroxide MRI contrast agents capable of tumor imaging over long time periods using clinical high-field ^{1}H MRI techniques.

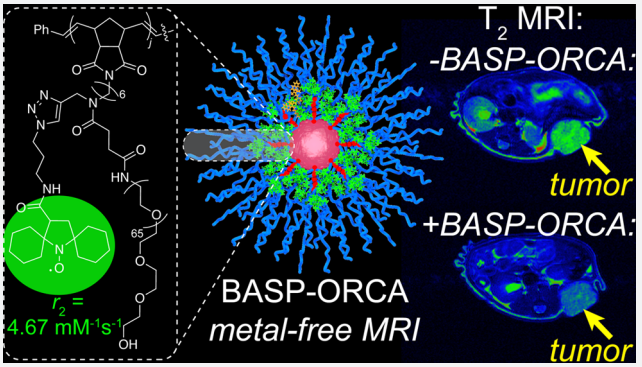

INTRODUCTION

Among the many imaging modalities for medical diagnostics, magnetic resonance imaging (MRI) is one of the most useful thanks to its ability to noninvasively generate three-dimensional detailed anatomical images with high spatial resolution while not requiring an ionizing source and remaining insensitive to depth.[1−4] Current clinical MRI methods depict the spatial distribution and chemical environment of water protons (^{1}H) within a region of interest (ROI); to enhance the differences between native water ^{1}H and ROIs, contrast agents are often employed. These contrast agents are divided into two primary classes: T_1 contrast agents (e.g., paramagnetic metals such as gadolinium or manganese) that afford positive-contrast images primarily by locally reducing the water ^{1}H longitudinal relaxation time (spin−lattice, T_1), and T_2 contrast agents (e.g., superparamagnetic iron oxide nanoparticles) that afford negative-contrast images by locally reducing the water ^{1}H transverse relaxation time (spin−spin, T_2).[5,6] The corresponding water ^{1}H relaxivities (r_1 and r_2, respectively) of a contrast agent characterize the extent to which the agent decreases the T_1 and T_2 times of water ^{1}H. Contrast agents with greater r_1 and r_2 values provide increased image contrast compared to those with lower values at the same concentration.[6,7]

Most MRI contrast agents with large r_1 and/or r_2 values contain metals that possess several unpaired electrons. For example, small molecule[8−13] and nanoparticle-based[14−21] contrast agents featuring Gd, Mn, Fe-oxide, and other metals have been reported to function as either T_1 or T_2 contrast agents or both. Furthermore, metal-based contrast agents that display advanced functions such as multimodal imaging,[8−10,12,13,17,20,21] enhanced target-specific accumulation,[14,18,19] and/or sensing[8,11−14] have been developed. Despite their unquestionable utility, metal-based contrast agents, especially nanoparticle ones that tend to accumulate in biological tissues, may present toxicity concerns in some

Received: June 14, 2017
Published: July 12, 2017

DOI: 10.1021/acscentsci.7b00253
ACS Cent. Sci. 2017, 3, 800−811

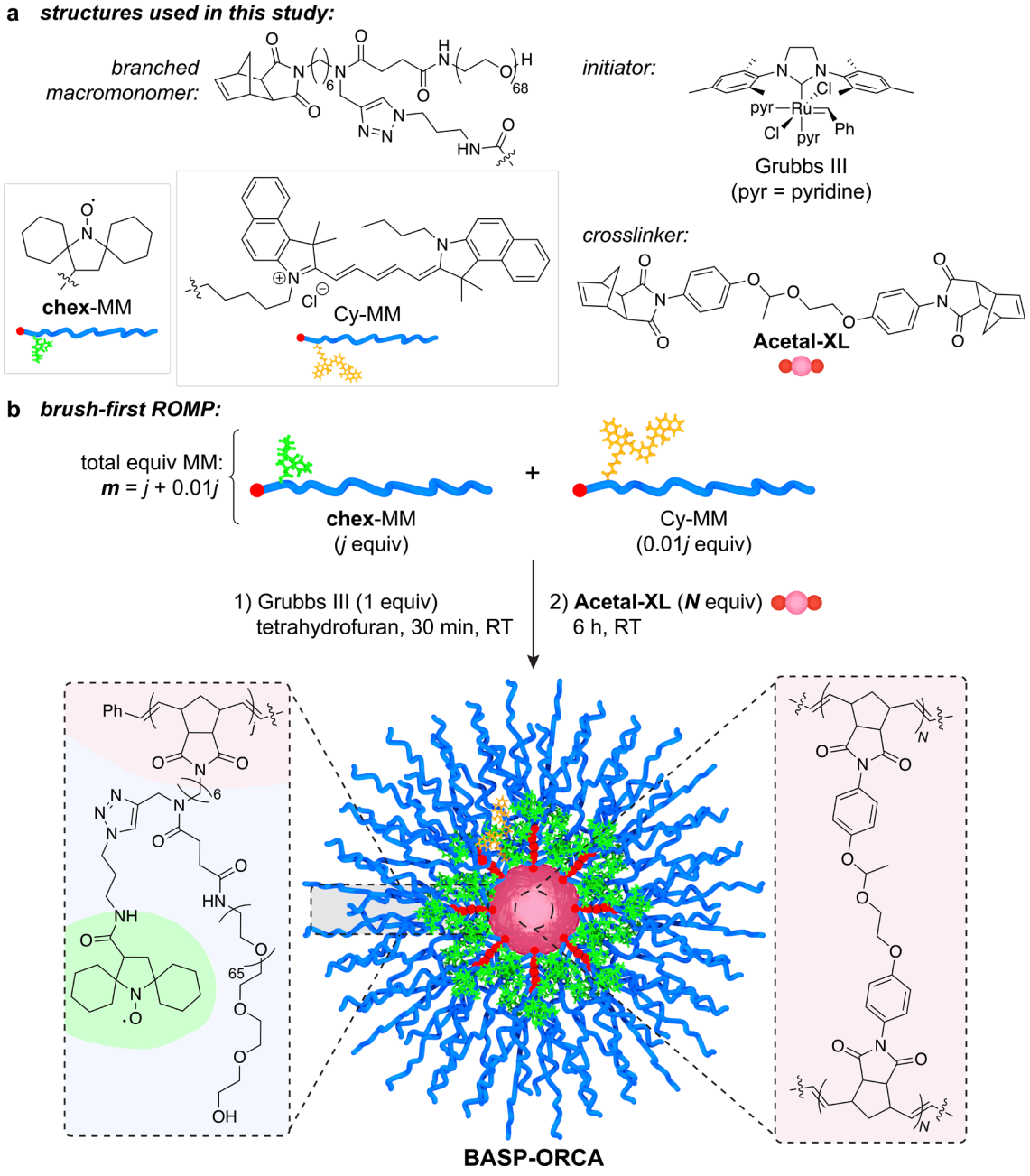

Figure 1. (a) Chemical structures of BASP components studied in this work. (b) General brush-first ROMP procedure. Branched MMs **chex**-MM and Cy-MM are combined in the ratio j : 0.01j. This combination of MMs is exposed to 1.0 equiv of Grubbs III initiator to produce a living bottlebrush with an average degree of polymerization (DP) = j + 0.01j = m. N equiv of **acetal-XL** is then added (in aliquots of 5 equiv of **acetal-XL** every 5 min) to provide the final BASP-ORCA. The properties of the BASP-ORCAs are defined by their m and N values (Table 1).

patient populations. For example, Gd-based agents, perhaps the most widely used T_1 contrast agents in the clinic, are associated with potentially lethal nephrogenic systemic fibrosis, and they have recently been linked to a rising prevalence of toxic Gd ions in the environment.[5,22−28] In addition, several T_2 contrast agents based on Fe-nanoparticles have been stopped from further development or withdrawn from the market due to safety concerns.[29−32] Moreover, according to the FDA, Fe-based products including ferumoxytol (Feraheme), the only FDA-approved superparamagnetic iron oxide nanoparticle currently available on the market, carry a risk of potentially life-threatening allergic reactions.[33−35] Thus, there is extensive interest in the development of "metal-free" MRI contrast agents that make use of entirely organic-based components. Such agents could enable MRI in at-risk patient populations, and they could potentially open new avenues for functional/responsive MRI based on *in vivo* organic transformations. Furthermore, organic nanoparticle contrast agents could provide safe alternatives in MR imaging applications that may require long-term tissue accumulation, such as tumor imaging.

Four main classes of metal-free MRI contrast agents have been the most widely studied: paramagnetic nitroxide-based organic radical contrast agents (ORCAs), hyperpolarized ^{13}C agents, ^{19}F MRI contrast agents, and chemical exchange saturation transfer (CEST) contrast agents. While ^{19}F MRI and CEST agents have undergone many advances in recent

DOI: 10.1021/acscentsci.7b00253
ACS Cent. Sci. 2017, 3, 800−811

Table 1. Characterization Data for BASP-ORCAs and Control Compounds

	composition		diameter		relaxivity		
name	*m*	*N*	D_h/nm	D_{TEM}/nm	r_1/mM^{-1} s^{-1}	r_2/mM^{-1} s^{-1}	notes
3-CP[a]					0.15	0.17	
chex-MM[b]					0.21	0.30	
chex-dendrimer[a]					0.44	0.86	
chex-bottlebrush[b]	55.55		17[b]	n.d.	0.32	0.82	
BASP-ORCA	5.05	20	31 ± 2	n.d.	0.27	6.92	poor solubility (<10 mg/mL)
BASP-ORCA	5.05	30	49 ± 6	n.d.	0.53	7.11	poor solubility (<10 mg/mL)
BASP-ORCA1	*7.07*	*20*	*31 ± 4*	*37 ± 7*	*0.41*	*4.67*	*good solubility (>50 mg/mL)*
BASP-ORCA	7.07	30	36 ± 3	n.d.	0.35	7.40	poor solubility (<10 mg/mL)
BASP-ORCA	9.99	15	28 ± 3	38 ± 10	0.33	2.90	low relaxivity
BASP-ORCA	9.99	30	33 ± 4	39 ± 10	0.37	4.52	low relaxivity

[a]From refs 52 and 53. [b]From ref 80.

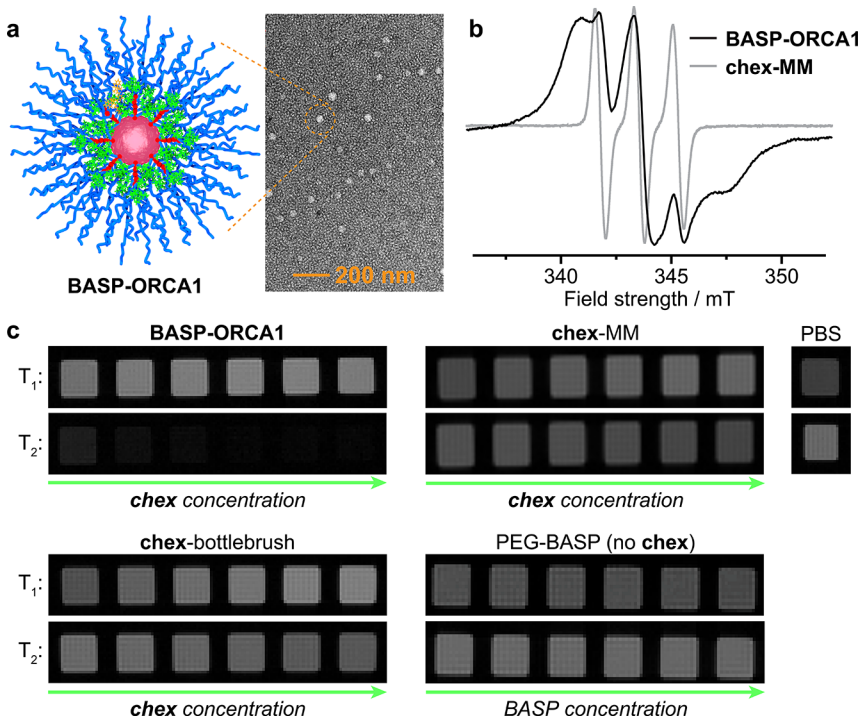

Figure 2. (a) Transmission electron microscopy image of **BASP-ORCA1** (D_{TEM} = 37 ± 7 nm) after being negatively stained with uranyl acetate; the reported diameter (D_{TEM}) represents the mean and standard deviation of >150 individual particle measurements. (b) Electron paramagnetic resonance (EPR) spectra for **BASP-ORCA1** and **chex**-MM. (c) T_1 and T_2-weighted MRI phantoms for **BASP-ORCA1**, **chex**-MM, PBS buffer, **chex**-bottlebrush, and a PEG-BASP lacking **chex**. The concentration of **chex**-containing samples (**BASP-ORCA1**, **chex**-MM, and **chex**-bottlebrush) ranges from 1 mM to 4 mM **chex**. The concentration of PEG-BASP lacking **chex** ranges from 6 mg/mL to 21 mg/mL, which is equivalent to the mass per volume concentration range of **BASP-ORCA1**.

years,[36−43] these approaches often suffer from low sensitivity, and in some cases, require a high contrast agent concentration (10−50 mM), long imaging times, and/or potentially harmful high-intensity radio frequency fields. Hyperpolarized ^{13}C agents, on the other hand, can theoretically afford up to 10^5 sensitivity improvements; nevertheless, issues including short hyperpolarization lifetimes that lead to limited imaging times, complexity in terms of the chemistry and instrumentation required for generation of the hyperpolarized agent, and a rather small substrate scope remain major challenges.[44−46] Furthermore, ^{19}F MRI, CEST, and hyperpolarized ^{13}C agents rely on imaging mechanisms that are not currently common in the clinic.[44−51] In contrast, nitroxide ORCAs rely on standard water relaxation mechanisms to achieve MRI contrast; they could in principle be immediately translated to clinical applications. However, several key challenges limit the clinical feasibility of nitroxide ORCAs. First, nitroxide radicals only possess one unpaired electron. As a result, compared to metal-based contrast agents such as Gd^{3+} (seven unpaired electrons) or Mn^{2+} (five unpaired electrons), nitroxide ORCAs inherently suffer from much lower water ^{1}H relaxivity. One strategy to achieve higher molecular relaxivity is to use a poly(nitroxide) where the relatively low per nitroxide relaxivity is multiplied by the number of nitroxides bound to a polymer scaffold. The second major limitation of nitroxide ORCAs is that they are typically reduced rapidly *in vivo* (half-lives on the order of minutes) to diamagnetic hydroxylamines, thus rendering them ineffective as contrast agents shortly after injection.[52−55] Initial efforts to utilize nitroxides as MRI contrast agents exposed these shortcomings,[56,57] and though their rapid bioreduction

DOI: 10.1021/acscentsci.7b00253
ACS Cent. Sci. 2017, 3, 800−811

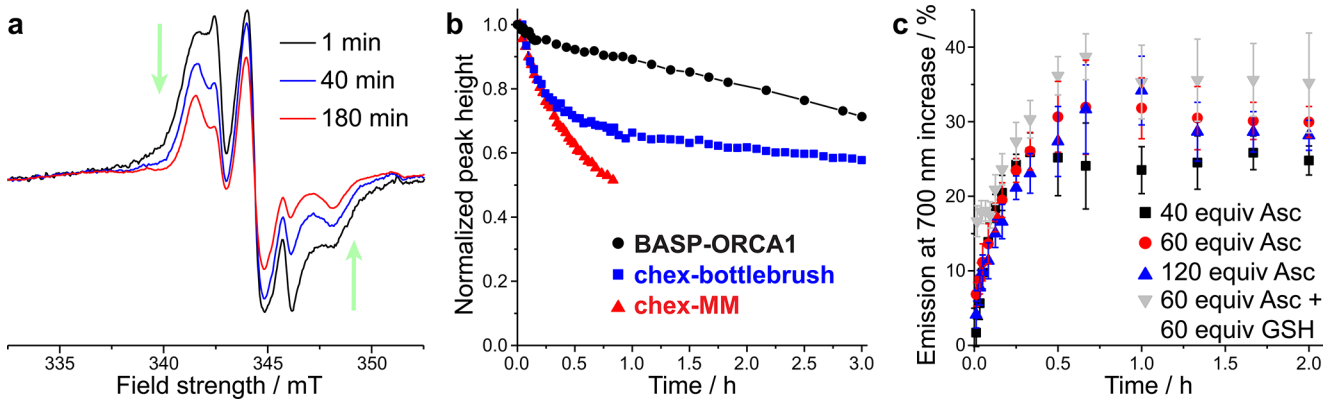

Figure 3. (a) EPR spectra for **BASP-ORCA1** 1, 40, and 180 min following exposure to 20 equiv of sodium ascorbate (Asc) per nitroxide. (b) Ascorbate reduction kinetics for **BASP-ORCA1**, **chex**-bottlebrush, and **chex**-MM. (c) Cy5.5 emission at 700 nm in response to Asc and glutathione (GSH); the reported values represent the mean and standard error of the mean (SEM) (n = 3).

has been cleverly exploited to enable redox-mapping *in vitro* and *in vivo*,[58−62] an *in vivo*-stable nitroxide ORCA that allows for longitudinal studies over clinically meaningful time scales following systemic administration has yet to be developed.

Macromolecular nitroxide ORCAs with long-term *in vivo* stability could be particularly useful for tumor imaging. Nanoparticles of suitable size (∼10−200 nm) are known to passively accumulate in tumors, especially in murine models, via the enhanced permeation and retention effect, but hours to tens of hours are often needed to reach maximal accumulation.[63−69] To our knowledge, there are no nitroxide-based molecules or materials with demonstrated capability to provide *in vivo* MRI contrast after such long times. This problem is exacerbated in murine models where imaging is often used for preclinical studies of disease development: murine tissues contain higher levels of metabolic antioxidants, which lead to faster nitroxide reduction rates.[70,71] Thus, the development of stable nitroxide-based macromolecular ORCAs with high relaxivities could open a new arena of MRI applications, whereby the accumulation of contrast agents in diseased tissues could be monitored by MRI without off-site toxicity concerns.[55,72,73] Moreover, the synthetic versatility of polymeric materials could facilitate future image-guided drug delivery strategies.

Herein, we report the design, synthesis, and biological evaluation of a new class of nitroxide macromolecules—brush-arm star polymer ORCAs (BASP-ORCAs)—with unique structures that are designed to overcome the aforementioned challenges associated with tumor MRI with nitroxide-based contrast agents. BASP-ORCAs contain a high concentration of reduction-resistant nitroxide groups bound in an interlayer between a poly(ethylene glycol) (PEG) shell and a polyacetal core. Due to their shielded and dense nitroxide layer, yet hydrophilic PEGylated nanostructures, BASP-ORCAs simultaneously possess the highest known water ^{1}H transverse relaxivities and stabilities for nitroxide ORCAs. In addition, the modularity of BASP synthesis was exploited to install near-infrared fluorophores into BASP-ORCAs and thereby achieve near-infrared fluorescence (NIRF) imaging in concert with MRI. Leveraging this combination of features, BASP-ORCAs were successfully employed for longitudinal MR and NIRF imaging of tumors with MRI contrast enhancement on par with metal-based contrast agents observed up to 1 day following systemic administration, which has, to our knowledge, never been achieved with a paramagnetic organic agent. Notably, though previous studies on nitroxide MRI contrast agents focused on T_1-weighted imaging, BASP-ORCAs operate most effectively as T_2 contrast agents, which is advantageous given that high-field instruments are being increasingly adopted in the clinic, and r_2 often remains similar or increases with magnetic field strength.[74] Thus, BASP-ORCAs not only overcome the challenges that have plagued all previous nitroxide-based MRI contrast agents, and thereby facilitate the first longitudinal imaging of tumors with a nitroxide ORCA, but they are also naturally amenable to current and future clinical high-field MRI instruments.

RESULTS AND DISCUSSION

BASP-ORCA Design and Synthesis. One of the most common ways to increase the relaxivity of MRI contrast agents (including nitroxides) involves attaching them to a rigid macromolecular scaffold.[6,47,52,53,75−78] For example, Rajca and co-workers appended a spirocyclohexyl nitroxide derivative ("**chex**")[79] to the surface of dendrimers to produce **chex**-dendrimer ORCAs where the per-**chex** r_1 was 0.42 mM^{-1} s^{-1} compared to r_1 = 0.14 mM^{-1} s^{-1} for the model nitroxide 3-carboxy-2,2,5,5-tetramethyl-l-pyrrolidinyloxy (**3-CP**).[52,53] In a later study, we appended **chex** to the core of PEGylated branched-bottlebrush polymers.[80] The resulting "**chex**-bottlebrush" had a per-**chex** r_1 of 0.32 mM^{-1} s^{-1}, which was

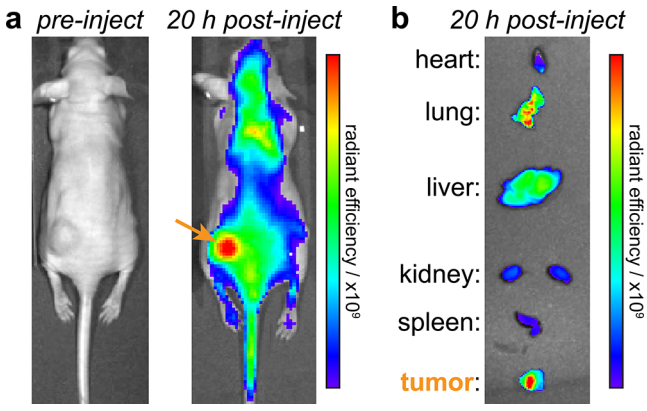

Figure 4. (a) *In vivo* NIRF images of NCR nude mouse before and 20 h after injection of **BASP-ORCA1** (see Supporting Information for details). (b) *Ex vivo* NIRF images of selected organs (see Supporting Information for details). Units of radiant efficiency: $\frac{\text{p / sec / cm}^2\text{ / sr}}{\mu\text{W / cm}^2}$.

DOI: 10.1021/acscentsci.7b00253
ACS Cent. Sci. 2017, 3, 800−811

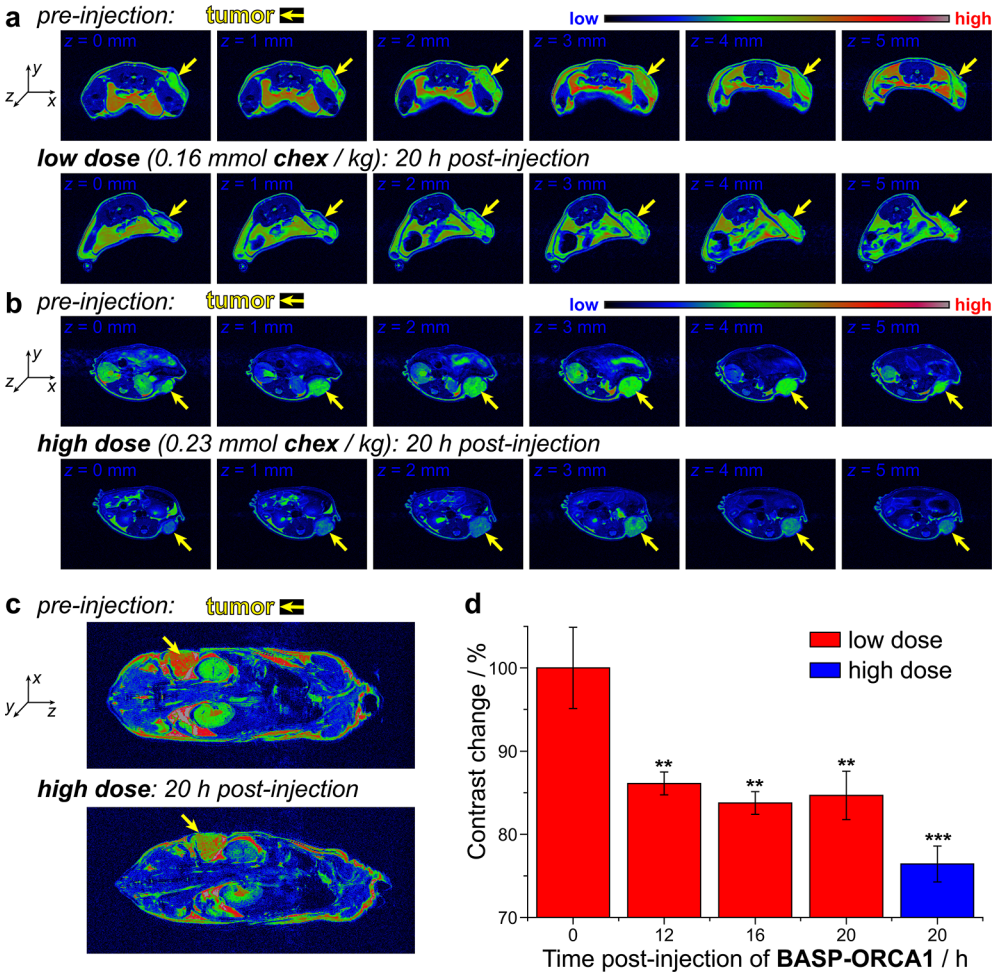

Figure 5. (a) T_2-weighted MR images of tumor bearing NCR nude mouse before (top row) and 20 h after (bottom row) injection of 0.16 mmol **chex**/kg ("low dose") of **BASP-ORCA1**. Each series of images corresponds to progressive slices in the *z*-axis through the tumor of the same mouse. (b) T_2-weighted MR images of tumor bearing NCR nude mouse before (top row) and 20 h after (bottom row) injection of 0.23 mmol **chex**/kg ("high dose") of **BASP-ORCA1**. Each series of images corresponds to progressive slices in the *z*-axis through the tumor of the same mouse. (c) T_2-weighted coronal MR images before (top) and 20 h after (bottom) injection of 0.23 mmol **chex**/kg ("high dose") of **BASP-ORCA1**. (d) Percent MRI contrast change at various times following **BASP-ORCA1** injection compared to preinjection. Statistical comparisons (n = 3 for low dose group; n = 4 for high dose group; reported values represent mean ± SEM) to preinjection images were made with a student t test: $^{**}P \leq 0.05$, $^{***}P \leq 0.001$.

approximately 50% greater than the **chex**-macromonomer used to synthesize these polymers (**chex**-MM, Figure 1a). In this system, r_2 also increased from 0.30 mM^{-1} s^{-1} for **chex**-MM to 0.82 mM^{-1} s^{-1} for the **chex**-bottlebrush polymer, thus demonstrating that increasing the macromolecular size and **chex** density leads to increases in both r_1 and r_2, with a greater increase in r_2.[80] In an effort to further increase these relaxivity values, we sought to incorporate **chex** into our BASP macromolecules wherein the nitroxides would be bound at a rigid core−shell interface.[80−83] On the basis of this novel structure compared to previous systems, we hypothesized that BASPs could provide enhanced relaxivity and nitroxide stability potentially making tumor imaging *in vivo* possible. Moreover, the control and robustness of BASP synthesis would enable the scalable production of BASP-ORCAs with optimal sizes for tumor accumulation, which is difficult with previous macromolecular systems such as dendrimers and bottlebrush polymers.[84−86]

BASP-ORCAs were synthesized by brush-first ring-opening metathesis polymerization (ROMP) as depicted in Figure 1.[84,86−88] Norbornene-based branched macromonomers (MMs, Figure 1a) featuring 3 kDa PEG and either **chex** (**chex**-MM) or Cy5.5 dye (Cy-MM, Figure 1a) were copolymerized by exposure to Grubbs third-generation bis-pyridine initiator[89] (Grubbs III, Figure 1a; reaction stoichiometry: j equiv. **chex**-MM to 0.01j Cy-MM to 1.0 Grubbs III) for 30 min (Figure 1b). The resulting living bottlebrush polymers with an average degree of polymerization (DP) of $\sim j + 0.01j = m$ were then cross-linked via portionwise addition of N equiv of bis-norbornene acetal cross-linker **acetal-XL**[84] (Figure 1a) to the reaction mixture to generate the desired BASP-ORCA (Figure 1b). With this method, the BASP-ORCA size is determined by the MM to Grubbs III to **acetal-XL** ratios (i.e., m and N values). Much less Cy-MM (0.01j) relative to **chex**-MM (j) was used to bridge the difference in concentration requirements between MRI (mM to μM) and NIRF (nM to pM).[1,6]

To identify optimal conditions for the synthesis of BASP-ORCAs with narrow size distributions and average diameters of ∼25−40 nm, as well as high water solubility and relaxivity, we screened m and N values from 5−10 and 15−30, respectively (Table 1). Gel permeation chromatography (GPC) revealed nearly quantitative MM-to-bottlebrush conversion as well as

DOI: 10.1021/acscentsci.7b00253
ACS Cent. Sci. 2017, 3, 800−811

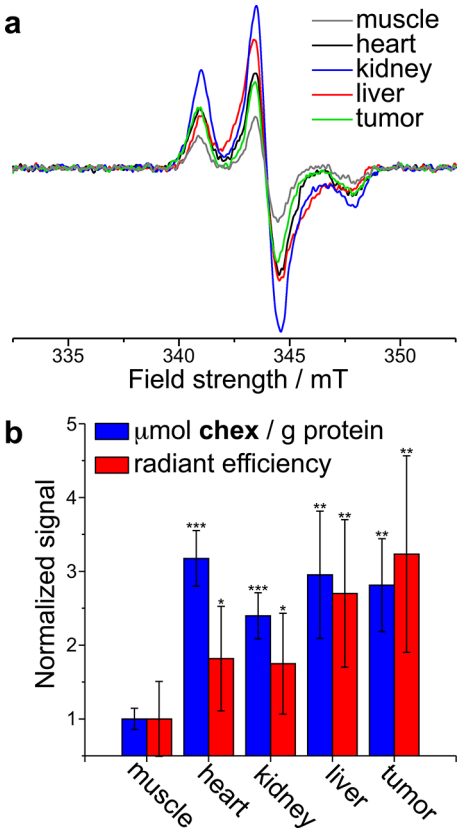

Figure 6. (a) EPR spectra obtained for homogenized tissue samples collected for the same mice imaged in Figure 5 22 h following **BASP-ORCA1** injection. (b) Blue: Muscle-normalized concentration of **chex** per gram of protein as obtained from EPR double integration of tissue homogenates. Red: Muscle-normalized concentration of Cy5.5 in tissue homogenates as obtained from NIRF imaging. Statistical comparisons (n = 4; reported values represent mean ± SEM) to muscle signal were made with a Student's t test: *not significant, **$P \leq 0.05$, ***$P \leq 0.001$.

≥85% bottlebrush-to-BASP conversion for all m and N values (Figure S1). The BASP-ORCA diameters as determined by dynamic light scattering (DLS) and transmission electron microscopy (TEM) ranged from ∼28 to ∼49 nm (Table 1). In general, for the same bottlebrush arm length (m), the BASP-ORCA size increased with the amount of **acetal-XL** added (N). In addition, the BASP-ORCA aqueous solubility (Table 1) increased with m. A representative TEM image for the m = 7.07 and N = 20 BASP-ORCA (referred to as **BASP-ORCA1** throughout the remainder of this work) is provided in Figure 2a. The aqueous solubility of **BASP-ORCA1** was the highest amongst the BASP-ORCAs prepared, and its hydrodynamic diameter (D_h) of 31 ± 4 nm is suitable for extended *in vivo* circulation and tumor accumulation.[66−68]

Characterization of BASP-ORCA Magnetic Properties. Electron paramagnetic resonance spectroscopy (EPR) was used to confirm the presence of **chex** in BASP-ORCAs, as well as to study the **chex** environment in **BASP-ORCA1**. The spin concentrations were ≥85% for all BASP-ORCAs. The height-normalized EPR spectra for **BASP-ORCA1** and **chex**-MM[80] are shown in Figure 2b. The spectrum for **BASP-ORCA1** is significantly broader than **chex**-MM, which is consistent with the larger and more rigid BASP nanostructure where **chex** is bound at the dense interface between the acetal cross-linker core and the PEG shell (Figures 1b and 2b). The **BASP-ORCA1** spectrum was simulated using the procedure developed by Budil, Freed, and co-workers[90] (see Supporting Information section A for details), which allows for characterization of the **chex** mobility in terms of the correlation time for rotational diffusion (τ). The spectrum was best fitted by superimposing two computed components (Figure S3): 22% corresponded to a relatively fast-moving nitroxide with τ = 0.2 ns, while 78% corresponded to a slow-moving nitroxide with τ = 10.0 ns. The faster-moving component likely corresponds to nitroxides that are furthest from the **BASP-ORCA1** acetal core (Figure 1b), while the slow-moving component corresponds to nitroxides that are close to and/or entangled within the acetal core. Notably, the τ of 10.0 ns measured for the slow component in **BASP-ORCA1** is quite large, which suggests that a majority of the **chex** groups are in a rigid environment. For comparison, in our previously reported **chex**-dendrimer ORCAs,[52,53] TEMPO-labeled bottlebrush polymers,[81,82] and BASPs,[83] the largest τ measured was ∼1 ns.

Next, we evaluated the longitudinal (r_1) and transverse (r_2) relaxivities of these BASP-ORCAs using a Bruker 7 T MRI scanner. The per-**chex** r_1 values as a function of m and N (Table 1) ranged from 0.27 to 0.53 mM^{-1} s^{-1}; they were not significantly increased compared to Rajca's **chex**-dendrimer and our **chex**-bottlebrush polymers. However, the per-**chex** r_2 values ranged from 2.90 to 7.40 mM^{-1} s^{-1}, which is ∼3.5- to ∼9.0-fold greater than the per-**chex** r_2 in our **chex**-bottlebrush polymers and ∼17- to ∼44-fold greater than **3-CP** (Table 1).[80] **BASP-ORCA1** displayed a per-**chex** r_2 value of 4.67 mM^{-1} s^{-1}. Though this value was not the highest we measured, we selected **BASP-ORCA1** for translation to biological studies because it offered the best balance of high relaxivity, solubility (greater than 50 mg/mL, Table 1), and size. Given the number-average molar mass of **BASP-ORCA1** as determined by gel permeation chromatography and static light scattering (M_n = 4.75 × 10^5 g/mol, $Đ$ = 1.32), we estimate that each **BASP-ORCA1** particle contains an average of 92 **chex** groups. Thus, the estimated average molecular r_1 and r_2 values for **BASP-ORCA1** are 37.6 mM^{-1} s^{-1} and 428.8 mM^{-1} s^{-1}, respectively, which are greater than those for the commonly used FDA-approved Gd-based contrast agent Magnevist (r_1 = 3.1 mM^{-1} s^{-1} and r_2 = 5.4 mM^{-1} s^{-1} at 7 T) and iron-based nanoparticles such as Feraheme (r_1 = 3.1 mM^{-1} s^{-1} and r_2 = 68 mM^{-1} s^{-1} at 7 T).[91−94]

MR phantom images of phosphate-buffered saline (PBS) solutions of **BASP-ORCA1**, **chex**-MM, and our previously reported **chex**-bottlebrush polymer at various **chex** concentrations (from 1 mM−4 mM **chex**) as well as a PEG-BASP that lacks **chex** (at equivalent mass fractions to **BASP-ORCA1**) are provided in (Figure 2c), along with images for "blank" PBS buffer. The T_1-weighted images for **BASP-ORCA1**, and **chex**-bottlebrush polymer are not obviously different, while the T_2-weighted images clearly show a large reduction in signal for **BASP-ORCA1**. The PEG-BASP with no **chex** shows no difference in contrast as a function of concentration, which confirms that **chex** is required to observe changes in image contrast.

The data presented above demonstrate that the high nitroxide density of **BASP-ORCA1**, which is a consequence of its unique cross-linked multilayer nanostructure, affords an increased magnetization capability that leads to r_2 enhancement. This finding is consistent with reports where nitroxides are utilized as magnetic catalysts for outer-sphere relaxation processes.[95−97] Most importantly, the exceptionally high r_2 of

DOI: 10.1021/acscentsci.7b00253
ACS Cent. Sci. 2017, 3, 800−811

BASP-ORCA1 overcomes one of the major limitations of nitroxide-based contrast agents: inherently low contrast.

Ascorbate Quenching Kinetics of BASP-ORCAs. As discussed above, nitroxide-based ORCAs typically suffer from rapid reduction to diamagnetic hydroxylamines under biologically relevant conditions. Among the many potential biological reducing agents, ascorbate (Asc) is known to play a major role in *in vivo* nitroxide reduction,[54,98,99] and Asc-induced reduction can be amplified by glutathione (GSH).[80,99] We hypothesized that the rigid **chex** environment in our BASP-ORCAs could help to lower the rate of **chex** reduction. To test this hypothesis, we collected EPR spectra for **BASP-ORCA1** at various times following exposure to 20 equiv of Asc and 20 equiv of GSH per nitroxide (both reagents were present in 10 mM concentrations). EPR spectra collected 1, 40, and 180 min after exposure to these conditions are provided in Figure 3a. The changes in peak height as a function of time are indicative of nitroxide reduction. The normalized peak height of the EPR spectra are plotted versus time in Figure 3b. Reduction kinetics data for our previous **chex**-bottlebrush polymers and **chex**-MM are provided for comparison.[80] In contrast to the **chex**-bottlebrush and **chex**-MM samples, which both display an initial rapid **chex** reduction phase in the first hour, the reduction of **chex** in **BASP-ORCA1** was significantly retarded with nearly 85% remaining after 1 h, and 70% remaining after 3 h (compared to 65% and 57%, respectively, for the **chex**-bottlebrush). On the basis of the integrated peak heights as a function of time, the second-order rate constants for **BASP-ORCA1** reduction in the initial (first 10 min) and late (>1 h) stages of the reduction process were calculated: k_{early} = 0.0376 M^{-1} s^{-1} and $k_{late} \approx$ 0.00672 M^{-1} s^{-1}) (Table S1).[52,53,80] Simulations revealed that the EPR spectra collected during the reduction process consisted of a "fast" and a "slow" component (Figure S3). Interestingly, τ for the "fast" component remained constant at 0.2 ns, while τ for the "slow" component became increasingly larger with time (11.0 ns at 40 min and 13.2 ns at 180 min). Therefore, even after 3 h there persists an extremely reduction resistant and slow moving nitroxide population. The presence of these very stable nitroxides within **BASP-ORCA1** may enable T_2-weighted MRI over longer time scales than have been possible with previous nitroxide contrast agents (*vide infra*).

Fluorescence Properties of BASP-ORCAs. As noted above, Cy5.5 was also incorporated into these BASP-ORCAs (see Figure S4 for **BASP-ORCA1** absorption and emission spectra confirming the presence of Cy5.5) in order to simultaneously use NIRF as an imaging modality for comparison to MRI. Nitroxides are well-known to quench fluorescence via catalysis of nonemissive photophysical processes such as intersystem crossing. This quenching requires close interaction between the nitroxide and the fluorophore; the systems with the greatest quenching typically feature the nitroxide directly linked to the fluorophore via π bonds (i.e., electronic conjugation).[100−102] Given the fact that **chex** and Cy5.5 are incorporated into BASP-ORCAs via two different macromonomers and that the mobility of **chex** is limited in these constructs, we reasoned that Cy5.5 quenching would be minimal; therefore, we could potentially use Cy5.5 emission as a fairly constant descriptor of particle concentration regardless of the extent of **chex** reduction.

To test this hypothesis, we exposed **BASP-ORCA1** to a large excess of Asc (40−120 equiv. to **chex**) in water, and monitored the resulting Cy5.5 emission. In agreement with our expectation, only a 25 ± 2% to 30 ± 2% increase in fluorescence emission was observed (Figure 3c). Moreover, addition of GSH (60 equiv) as a coreductant along with 60 equiv of Asc gave only a 35 ± 7% increase in fluorescence. Taken together, these data suggest that Cy5.5 fluorescence is minimally quenched by **chex** in **BASP-ORCA1**. For comparison, exposure of our previously reported **chex**-bottlebrush polymer containing Cy5.5 to excess Asc or Asc+GSH led to 119 ± 5% and 250 ± 5% increases in fluorescence, respectively.[80] Notably, the time required to achieve a fluorescence plateau varied significantly between **BASP-ORCA1** (approximately 40 min) and our **chex**-bottlebrush polymer (a few minutes). Collectively, these data suggest that the BASP nanostructure provides greater steric shielding and isolation of **chex** and Cy5.5 compared to the **chex**-bottlebrush polymer.

***In Vitro* Cytotoxicity and *in Vivo* Gross Toxicity, Pharmacokinetics (PK), and Biodistribution (BD) of BASP-ORCA1 in Non-Tumor-Bearing Mice.** Next, we investigated the performance of **BASP-ORCA1** in biological assays. As discussed above, one potential advantage of ORCAs is their low toxicity. To assess the toxicity of **BASP-ORCA1**, we first conducted *in vitro* human umbilical vein endothelial cell (HUVEC) and HeLa cell viability assays. In these assays, the cells were incubated with varied concentrations of **BASP-ORCA1** for 72 h. Cell viability was determined by the CellTiter-Glo assay (Supplemental Figure S5). The half-maximal inhibitory concentrations of **BASP-ORCA1**, i.e., the concentrations that led to 50% cell death, were 1.5 mg/mL (280 μM **chex**) and 4.5 mg/mL (830 μM **chex**) in HUVEC and HeLa cells, respectively. These results confirm that **BASP-ORCA1** induces negligible *in vitro* cytotoxicity at practical concentrations.[85,86] Next, the *in vivo* gross toxicity of **BASP-ORCA1** was assessed. Healthy BALB/c mice were administered increasing doses (from 5 to 30 mg or 0.2 to 1.5 g/kg, respectively) of **BASP-ORCA1** via tail vein injection. The animal body masses and behaviors were monitored over the course of 30 days. Loss of ≥10% body mass is generally considered to be a sign of unacceptable toxicity.[103,104] As shown in Figure S6, even the highest dose of **BASP-ORCA1** (administered to n = 4 animals) induced no significant decrease in body mass, which suggests that these particles are well-tolerated up to their solubility-limiting dose.

The pharmacokinetics (PK) and biodistribution (BD) of **BASP-ORCA1** were monitored in healthy, nontumor bearing BALB/c mice (n = 3) using NIRF imaging (IVIS, Cy5.5 $\lambda_{ex}/\lambda_{em}$ = 640/700 nm). For PK analysis, blood samples were collected via cardiac puncture at various time points from 1 to 48 h. Percent injected dose was plotted as a function of time (Figure S7a). As is common for spherical PEGylated nanostructures, **BASP-ORCA1** exhibited a two-phase clearance behavior, with an early distribution phase of ∼6 h, followed by a steady elimination phase.[67,86] Fitting the data presented in Figure S7a with a standard two-compartment model yielded a blood compartment half-life for **BASP-ORCA1** of 10 h.[105] This long half-life is attributed to the nanoscale size of **BASP-ORCA1**, which limits renal clearance, and its PEGylated corona.[66,69] Consistent with these results and a plethora of studies on PEGylated nanoparticles,[65−69] BD analysis revealed that a majority of **BASP-ORCA1** accumulated in the liver, with increasing accumulation over 72 h (Figure S7b). Less accumulation in the kidney and negligible accumulation in other tissues was observed. Fluorescence in extracted lung tissue is attributed to a high concentration of **BASP-ORCA1** in

DOI: 10.1021/acscentsci.7b00253
ACS Cent. Sci. 2017, 3, 800−811

the blood. Notably, fluorescence images of fecal samples (Figure S7c) suggest that **BASP-ORCA1** is ultimately cleared from the body via excretion.

BASP-ORCA1 BD in Tumor-Bearing Mice. Given the long circulation of **BASP-ORCA1**, we hypothesized that this particle would passively accumulate in subcutaneous tumors following systemic injection. To test this hypothesis, we first established a tumor model via subcutaneous injection of a mixture of 2.0×10^6 lung carcinoma cells (A549, ATCC), Matrigel, and PBS buffer into a hind flank of NCR-NU mice ($n = 4$). When the average tumor volume was ∼1 cm, **BASP-ORCA1** was administered at a dose of 0.23 mmol **chex**/kg (1.2 g **BASP-ORCA1**/kg) via tail vein injection. NIRF images collected 20 h after administration indicated substantial tumor accumulation of **BASP-ORCA1**, which is consistent with other reports for PEGylated nanoparticles of similar size including our related drug-conjugated BASPs (Figure 4a).[65,66,69,86] *Ex vivo* BD data were consistent with our studies on nontumor bearing BALB/c mice (i.e., liver accumulation and persistence in blood) with the addition of significant tumor accumulation (Figure 4b and Figure S8).

MRI and NIRF Imaging with BASP-ORCA1 in Tumor-Bearing Mice. The low toxicity, long circulation half-life, and tumor accumulation of **BASP-ORCA1**, along with its exceptional stability and relaxivity, suggested that this particle could be suitable for MRI of tumors following systemic injection and accumulation; a feat that, to our knowledge, has not yet been achieved with ORCAs. Two groups of A459 tumor-bearing NCR-NU mice were administered different doses of **BASP-ORCA1** via tail-vein injection: the "low dose" group ($n = 3$) received 0.16 mmol **chex**/kg (0.8 g **BASP-ORCA1**/kg), while the "high dose" group ($n = 4$) received 0.23 mmol **chex**/kg (1.2 g **BASP-ORCA1**/kg). The mice were anaesthetized and MR images were collected at various time points: 12, 16, and 20 h postinjection for the low dose group and 20 h postinjection for the high dose group. The images from each time point were compared to images collected before **BASP-ORCA1** injection. Figures 5a shows T_2-weighted false-colored images for a selected mouse from the low dose group imaged before **BASP-ORCA1** injection (top row of images) and 20 h (bottom row of images) after **BASP-ORCA1** injection. From left-to-right the images correspond to progressive slices of the same animal in the *z*-axis with the tumor indicated with a yellow arrow in each image. Figure 5b shows an analogous set of images for a selected mouse from the high dose group. Contrast differences between the preinjection and postinjection images can be observed at both dose levels, with greater contrast observed in the high dose animal (Figure 5b). Whole animal images similarly revealed a clear difference in tumor contrast (Figure 5c, yellow arrows).

The percent negative contrast enhancement (i.e., the amount of signal reduction) before and after **BASP-ORCA1** administration was quantified by image analysis (Figure 5d). Signal reductions ranging from 14 ± 2% to 16 ± 2% ($P \leq 0.05$) were observed for the 12 to 20 h time points in the low dose group (Figure 5d, red bars). In the high dose group, a 24 ± 2% ($P \leq 0.001$) signal reduction was observed 20 h after **BASP-ORCA1** administration (Figure 5d, blue bar). The **BASP-ORCA1** dose−response effect suggests that the observed contrast differences between pre- and postinjection are due to accumulation of **BASP-ORCA1** in the tumors. Keeping in mind that MRI phantoms revealed no observable contrast enhancement for PEG-BASPs that lack **chex** (Figure 2c), these MRI data imply that 20 h following injection there is a sufficient concentration of **chex** radicals present on the **BASP-ORCA1** in the tumor to impart contrast. To confirm the presence of **chex** radicals in the tumors, the same mice that were imaged by MRI were sacrificed 21 h after **BASP-ORCA1** administration and their tissue homogenates and blood were analyzed by EPR spectroscopy (Figure 6a). From these spectra, the radical concentration per gram of protein in each tissue sample, the latter obtained via a bicinchoninic acid assay (BCA), was evaluated and normalized by the radical concentration per gram of protein in muscle tissue (Figure 6b). In agreement with our MRI data, the concentration of free radicals in the tumor was quite high after **BASP-ORCA1** injection; the measured value of 0.25 ± 0.04 μmol chex/g **chex**/g of protein corresponds to 4.5% of the injected dose of **chex** radicals. Moreover, consistent with our *in vivo* NIRF imaging results (*vide supra*), relatively high radical concentrations were observed in the liver and kidney, which suggests that the clearance of **BASP-ORCA1** proceeded mostly through these organs. Notably, the murine liver contains a high concentration of Asc (millimolar range); our observation of radicals in the liver is further evidence of the extremely stable nature of the **chex** units in **BASP-ORCA1** (*Note:* in our previous **chex**-bottlebrush polymers, there was very little **chex** radical in the liver following 30 min and none observed after 24 h). A high **chex** concentration was also observed in the heart, which is in accord with a long blood compartment half-life and is consistent with our PK data obtained by NIRF imaging. Finally, NIRF imaging of these homogenates provided fluorescence radiant efficiencies that were in good agreement with our spin concentrations (Figure 6b), which suggests that the **chex** radicals and Cy5.5 dyes are still colocalized within the **BASP-ORCA1** construct after biodistribution. Unlike our previous **chex**-bottlebrush polymers, which displayed dramatic increases in fluorescence as **chex** was reduced, the signal uniformity offered by **BASP-ORCA1** provides for straightforward multimodal confirmation of BD.

To the best of our knowledge, **BASP-ORCA1** is the first nitroxide MRI contrast agent capable of providing significant contrast 20 h after injection, which is a testament to its unique structural features that combine optimal size for tumor accumulation with a high nitroxide density and stability. To set these results in context, we compared our data to recent literature examples of MRI-contrast agents that rely on metals to achieve tumor imaging following systemic administration. For example, Kataoka and co-workers recently reported on a new class of Gd-based nanoparticles (T_1 contrast agents) for MRI of tumors. In their study, a ∼40% contrast enhancement (at 0.05 mmol Gd/kg iv dose) was observed 4 h following injection into mice bearing subcutaneous C26 tumors. Notably, the commercially available small molecule contrast agent Gd-DTPA exhibited negligible contrast enhancement (at 0.23 mmol Gd/kg iv dose) after 4 h.[16] This example highlights the importance of a nanoparticle system for extended circulation and tumor imaging. The same group reported Fe-based nanoparticles (T_2 contrast agents) for tumor imaging in a similar murine model (subcutaneous C26 tumors). Here, an approximately 25% contrast difference was observed 24 h following intravenous administration of 0.45 mg Fe/kg. Notably, less than 10% contrast enhancement was observed using commercially available Resovist (at 0.45 mg Fe/kg intravenous dose).[15] It should be noted that the instrument parameters used to obtain T_2-weighted images in this work

DOI: 10.1021/acscentsci.7b00253
ACS Cent. Sci. 2017, 3, 800−811

were similar to those used above in our studies; thus, our results for **BASP-ORCA1** are on par with recently reported nanoparticle MRI contrast agents that rely on metals to achieve contrast.

CONCLUSION

We have developed a nitroxide-based macromolecular MRI contrast agent —**BASP-ORCA1**— that enables simultaneous MRI and NIRF imaging *in vivo* over time scales suitable for tumor imaging following systemic injection. **BASP-ORCA1** addresses the two major challenges that have historically limited nitroxide-based organic radical contrast agents for MRI: low relaxivity and poor stability. These functions were made possible by the brush-arm star polymer (BASP) nanostructure, which places a dense layer of **chex** nitroxides at the interface between a rigid poly(acetal) core and a hydrophilic PEG shell. Altogether, **BASP-ORCA1** displayed unprecedented per-nitroxide and per-molecule transverse relaxivities for organic radical contrast agents, exceptional stability, high water solubility, low *in vitro* and *in vivo* toxicity, and a long blood compartment half-life. These features combined to facilitate the imaging of subcutaneous tumors in mice 20 h after tail-vein injection, providing contrast enhancements on par with commercial and literature examples of metal-based contrast agents. This work suggests that organic radicals can be viable alternatives to metal-based MRI contrast agents, and sets the stage for the development of theranostic systems that combine organic radical contrast agents with therapeutic payloads to achieve simultaneous tumor imaging and drug delivery without concerns over long-term tissue accumulation of metals.

ASSOCIATED CONTENT

Supporting Information

The Supporting Information is available free of charge on the ACS Publications website at DOI: 10.1021/acscentsci.7b00253.

Synthesis and characterization data for BASPs, as well as supplementary figures, methods and materials, experimental procedures, *in vitro*, *in vivo*, and *ex vivo* supplementary data (PDF)

AUTHOR INFORMATION

Corresponding Author

*E-mail: jaj2109@mit.edu.

ORCID

Qixian Chen: 0000-0002-3091-671X

M. Francesca Ottaviani: 0000-0002-4681-4718

Andrzej Rajca: 0000-0002-8856-1536

Jeremiah A. Johnson: 0000-0001-9157-6491

Notes

The authors declare no competing financial interest.

ACKNOWLEDGMENTS

We thank the NIH-NIBIB (1R21EB018529-01A1 for J.A.J. and A.R.; R01 EB-019950-01A1 for A.R.) and the National Science Foundation (Graduate Research Fellowship for H.V.-T.N.) for support of this research. A.J. thanks the NIH (U01-NS090451). P.H. was supported by a Wellcome Trust-MIT Postdoctoral Fellowship. This work was supported in part by the Koch Institute Support (core) Grant P30-CA14051 from the National Cancer Institute. We thank the Koch Institute Swanson Biotechnology Center for technical support, specifically Dr. S. Malstrom and Ms. W. Huang. We thank Dr. A. Detappe and Dr. P. Ghoroghchian for very fruitful discussions and consultations.

DEDICATION

[¶]We dedicate this work to our co-author, Michael D. Boska, who passed away on May 13, 2017 in a one-man hang glider accident. Hang gliding was Mike's hobby and his dream come true for nearly 40 years. He spent his last moments doing what he loved. This loss is tremendous on multiple levels. Mike was an incredible asset to our research, the community, and the University of Nebraska Medical Center. His contributions will positively impact the medical field for years to come.

REFERENCES

(1) Cheon, J.; Lee, J.-H. Synergistically Intergrated Nanoparticles as Multimodal Probes for Nanobiotechnology. *Acc. Chem. Res.* **2008**, *41*, 1630−1640.

(2) Na, H. B.; Song, I. C.; Hyeon, T. Inorganic Nanoparticles for MRI Contrast Agents. *Adv. Mater.* **2009**, *21*, 2133−2148.

(3) Lee, D.-E.; Koo, H.; Sun, I.-C.; Ryu, J. H.; Kim, K.; Kwon, I.-C. Multifunctional Nanoparticles for Multimodal Imaging and Theragnosis. *Chem. Soc. Rev.* **2012**, *41*, 2656−2672.

(4) Villaraza, A. J. L.; Bumb, A.; Brechbiel, M. W. Macromolecules, Dendrimers, and Nanomaterials in Magnetic Resonance Imaging: The Interplay between Size, Function, and Pharmacokinetics. *Chem. Rev.* **2010**, *110*, 2921−2959.

(5) Davies, G.-L.; Kramberger, I.; Davis, J. J. Environmentally Responsive MRI Contrast Agents. *Chem. Commun.* **2013**, *49*, 9704−9721.

(6) Mastarone, D. J.; Harrison, V. S. R.; Eckermann, A. L.; Parigi, G.; Luchinat, C.; Meade, T. J. A Modular System for the Synthesis of Multiplexed Magnetic Resonance Probes. *J. Am. Chem. Soc.* **2011**, *133*, 5329−5337.

(7) Caravan, P.; Ellison, J. J.; McMurry, T. J.; Lauffer, R. B. Gadolinium (III) Chelates as MRI Contrast Agents: Structure, Dynamics, and Applications. *Chem. Rev.* **1999**, *99*, 2293−2352.

(8) Tu, C.; Nagao, R.; Louie, A. Y. Multimodal Magnetic-resonance/Optical-imaging Contrast Agent Sensitive to NADH. *Angew. Chem., Int. Ed.* **2009**, *48*, 6547−6551.

(9) Harrison, V. S. R.; Carney, C. E.; MacRenaris, K. W.; Meade, T. J. A Multimeric MR-optical Contrast Agent for Multimodal Imaging. *Chem. Commun.* **2014**, *50*, 11469−11471.

(10) Harrison, V. S. R.; Carney, C. E.; MacRenaris, K. W.; Waters, E. A.; Meade, T. J. Multimeric Near IR-MR Contrast Agent for Multimodal *in vivo* Imaging. *J. Am. Chem. Soc.* **2015**, *137*, 9108−9116.

(11) MacRenaris, K. W.; Ma, Z.; Krueger, R. L.; Carney, C. E.; Meade, T. J. Cell-permeable Esterase-activated Ca(II)-Sensitive MRI Contrast Agent. *Bioconjugate Chem.* **2016**, *27*, 465−473.

(12) You, Y.; Tomat, E.; Hwang, K.; Atanasijevic, T.; Nam, W.; Jasanoff, A. P.; Lippard, S. Manganese Displacement from Zinpyr-1 Allows Zinc Detection by Fluorescence Microscopy and Magnetic Resonance Imaging. *Chem. Commun.* **2010**, *46*, 4139−4141.

(13) Zhang, X.; Jing, X.; Liu, T.; Han, G.; Li, H.; Duan, C. Dual-functional Gadolinium-based Copper(II) Probe for Selective Magnetic Resonance Imaging and Fluorescence Sensing. *Inorg. Chem.* **2012**, *51*, 2325−2331.

(14) Mi, P.; Kokuryo, D.; Cabral, H.; Wu, H.; Terada, Y.; Saga, T.; Aoki, I.; Nishiyama, N.; Kataoka, K. A pH-activatable Nanoparticle with Signal-aplification Capabilities for non-invasive Imaging of Tumor Malignancy. *Nat. Nanotechnol.* **2016**, *11*, 724−730.

(15) Kokuryo, D.; Anraku, Y.; Kishimura, A.; Tanaka, S.; Kano, M. R.; Kershaw, J.; Nishiyama, N.; Saga, T.; Aoki, I.; Kataoka, K. SPIO-PICsome: Development of a Highly Sensitive and Stealth-capable MRI Nano-agent for Tumor Detection using SPIO-loaded Unilamellar Polyion Complex Vesicles (PICsomes). *J. Controlled Release* **2013**, *169*, 220−227.

DOI: 10.1021/acscentsci.7b00253
ACS Cent. Sci. 2017, 3, 800−811

(16) Mi, P.; Kokuryo, D.; Cabral, H.; Kumagai, M.; Nomoto, T.; Aoki, I.; Terada, Y.; Kishimura, A.; Nishiyama, N.; Kataoka, K. Hydrothermally Synthesized PEGylated Calcium Phosphate Nanoparticles Incorporating Gd-DTPA for Contrast Enhanced MRI Diagnosis of Solid Tumors. *J. Controlled Release* **2014**, *174*, 63−71.
(17) Chou, S.-W.; Shau, Y.-H.; Wu, P.-C.; Yang, Y.-S.; Shieh, D.-B.; Chen, C.-C. *in vitro* and *in vivo* Studies of FePt Nanoparticles for Dual Modal CT/MRI Molecular Imaging. *J. Am. Chem. Soc.* **2010**, *132*, 13270−13278.
(18) Holbrook, R. J.; Rammohan, N.; Rotz, M. W.; MacRenaris, K. W.; Preslar, A. T.; Meade, T. J. Gd(III)-dithiolane Gold Nanoparticles for T1-Weighted Magnetic Resonance Imaging of the Pancreas. *Nano Lett.* **2016**, *16*, 3202−3209.
(19) Nicholls, F. J.; Rotz, M. W.; Ghuman, H.; MacRenaris, K. W.; Meade, T. J.; Modo, M. DNA-gadolinium-gold Nanoparticles for *in vivo* T1MR Imaging of Transplanted Human Neural Stem Cells. *Biomaterials* **2016**, *77*, 291−306.
(20) Choi, J.-S.; Lee, J.-H.; Shin, T.-H.; Song, H.-T.; Kim, E. Y.; Cheon, J. Self-confirming "AND" Logic Nanoparticles for Fault-free MRI. *J. Am. Chem. Soc.* **2010**, *132*, 11015−11017.
(21) Medarova, Z.; Pham, W.; Farrar, C.; Petkova, V.; Moore, A. *in vivo* Imaging of siRNA Delivery and Silencing in Tumors. *Nat. Med.* **2007**, *13*, 372−377.
(22) Shellock, F. G.; Kanal, E. Safety of Magnetic Resonance Imaging Contrast Agents. *J. Magn. Reson. Imaging.* **1999**, *10*, 477−484.
(23) Swaminathan, S.; Horn, T. D.; Pellowski, D.; Abul-Ezz, S.; Bornhorst, J. A.; et al. Nephrogenic Systemic Fibrosis, Gadolinium, and Iron Mobilization. *N. Engl. J. Med.* **2007**, *357*, 720−722.
(24) Shin, T.-H.; Choi, Y.; Kim, S.; Cheon, J. Recent Advances in Magnetic Nanoparticle-based Multi-modal Imaging. *Chem. Soc. Rev.* **2015**, *44*, 4501−4516.
(25) Verwilst, P.; Park, S.; Yoon, B.; Kim, J. S. Recent Advances in Gd-chelate Based Bimodal Optical/MRI Contrast Agents. *Chem. Soc. Rev.* **2015**, *44*, 1791−1806.
(26) Mendichovszky, I. A.; Marks, S. D.; Simcock, C. M.; Olsen, O. E. Gadolinium and Nephrogenic Systemic Fibrosis: Time to Tighten Practice. *Pediatr. Radiol.* **2008**, *38*, 489−496.
(27) Hatje, V.; Bruland, K. W.; Flegal, A. R. Increases in Anthropogenic Gadolinium Anomalies and Rare Earth Element Concentration in San Francisco Bay over a 20 Year Record. *Environ. Sci. Technol.* **2016**, *50*, 4159−4168.
(28) Nardone, B.; Saddleton, E.; Laumann, A. E.; Edwards, B. J.; Raisch, D. W.; McKoy, J. M.; Belknap, S. M.; Bull, C.; Haryani, A.; Cowper, S. E.; Abu-Alfa, A. K.; Miller, F. H.; Godinez-Puig, V.; Dharnidharka, V. R.; West, D. P. Pediatric Nephrogenic Systemic Fibrosis is Rarely Reported: a RADAR Report. *Pediatr. Radiol.* **2014**, *44*, 173−180.
(29) We thank one of the reviewers for pointing out to us safety issues associated with T_2 contrast agents based on iron-nanoparticles.
(30) Wang, Y-X. J. Superparamagnetic Iron Oxide Based MRI Contrast Agents: Current Status of Clinical Application. *Quant. Imaging. Med. Surg.* **2011**, *1*, 35−40.
(31) Wang, Y-X. J. Current Status of Superparamagnetic Iron Oxide Contrast Agents for Liver Magnetic Resonance Imaging. *World J. Gastroenterol.* **2015**, *21*, 13400−13402.
(32) Feng, J.; Liu, H.; Bhakoo, K. K.; Lu, L.; Chen, Z. A Metabonomic Analysis of Organ Specific Response to USPIO Administration. *Biomaterials* **2011**, *32*, 6558−6569.
(33) Vasanawala, S. S.; Nguyen, K.-L.; Hope, M. D.; Bridges, M. D.; Hope, T. A.; Reeder, S. B.; Bashir, M. R. Safety and Technique of Ferumoxytol Administration for MRI. *Magn. Reson. Med.* **2016**, *75*, 2107−2111.
(34) Thakor, A. S.; Jokerst, J. V.; Ghanouni, P.; Campbell, J. L.; Mittra, E.; Gambhir, S. S. Clinically Approved Nanoparticle Imaging Agents. *J. Nucl. Med.* **2016**, *57*, 1833−1837.
(35) *Feraheme (Ferumoxytol): Drug Safety Communication − Warnings Strengthened and Prescribing Instruction Changed*; U. S. Food & Drug Administration (FDA), 2015, https://www.fda.gov/safety/medwatch/safetyinformation/safetyalertsforhumanmedicalproducts/ucm440479.htm.
(36) Lim, Y. T.; Noh, Y.-W.; Cho, J.-H.; Han, J. H.; Choi, B. S.; Kwon, J.; Hong, K. S.; Gokarna, A.; Cho, Y.-H.; Chung, B. H. Multiplexed Imaging of Therapeutic Cells with Multispectrally Encoded Magnetofluorescent Nanocomposite Emulsions. *J. Am. Chem. Soc.* **2009**, *131*, 17145−17154.
(37) Rolfe, B. E.; Blakey, I.; Squires, O.; Peng, H.; Boase, N. R. B.; Alexander, C.; Parsons, P. G.; Boyle, G. M.; Whittaker, A. K.; Thurecht, K. J. Multimodal Polymer Nanoparticles with Combined 19F Magnetic Resonance and Optical Detection for Tunable, Targeted, Multimodal Imaging *in vivo*. *J. Am. Chem. Soc.* **2014**, *136*, 2413−2419.
(38) Patrick, M. J.; Janjic, J. M.; Teng, H.; O'Hear, M. R.; Brown, C. W.; Stokum, J. A.; Schmidt, B. F.; Ahrens, E. T.; Waggoner, A. S. Intracellular pH Measurements Using Perfluorocarbon Nanoemulsions. *J. Am. Chem. Soc.* **2013**, *135*, 18445−18457.
(39) Bar-Shir, A.; Yadav, N. N.; Gilad, A. A.; van Zijl, P. C. M.; McMahon, M. T.; Bulte, J. W. M. Single ^{19}F Probe for Simultaneous Detection of Multiple Metal Ions Using miCEST MRI. *J. Am. Chem. Soc.* **2015**, *137*, 78−81.
(40) Lock, L. L.; Li, Y.; Mao, X.; Chen, H.; Staedtke, V.; Bai, R.; Ma, W.; Lin, R.; Li, Y.; Liu, G.; Cui, H. One-component Supramolecular Filament Hydrogels as Theranostic Label-free Magnetic Resonance Imaging Agents. *ACS Nano* **2017**, *11*, 797−805.
(41) Ferrauto, G.; Di Gregorio, E.; Baroni, S.; Aime, S. Frequency-encoded MRI-CEST Agents Based on Paramagnetic Liposomes/RBC Aggregates. *Nano Lett.* **2014**, *14*, 6857−6862.
(42) Ratnakar, S. J.; Soesbe, T. C.; Lumata, L. L.; Do, Q. N.; Viswanathan, S.; Lin, C.-Y.; Sherry, A. D.; Kovacs, Z. Modulation of CEST Images *in vivo* by T_1 Relaxation: a New Approach in the Design of Responsive PARACEST Agents. *J. Am. Chem. Soc.* **2013**, *135*, 14904−14907.
(43) Ferrauto, G.; Delli Castelli, D.; Di Gregorio, E.; Langereis, S.; Burdinski, D.; Grull, H.; Terreno, E.; Aime, S. Lanthanide-loaded Erythrocytes as Highly Sensitive Chemical Exchange Saturation Transfer MRI Contrast Agents. *J. Am. Chem. Soc.* **2014**, *136*, 638−641.
(44) Terreno, E.; Castelli, D. D.; Viale, A.; Aime, S. Challenges for Molecular Magnetic Resonance Imaging. *Chem. Rev.* **2010**, *110*, 3019−3042.
(45) Glunde, K.; Artemov, D.; Penet, M.-F.; Jacobs, M. A.; Bhujwalla, Z. M. Magnetic Resonance Spectroscopy in Metabolic and Molecular Imaging and Diagnostic of Cancer. *Chem. Rev.* **2010**, *110*, 3043−3059.
(46) Smith, B. R.; Gambhir, S. S. Nanomaterials for In Vivo Imaging. *Chem. Rev.* **2017**, *117*, 901−986.
(47) Harvey, P.; Kuprov, I.; Parker, D. Lanthanide Complexes as Paramagnetic Probes for ^{19}F Magnetic Resonance. *Eur. J. Inorg. Chem.* **2012**, *2012*, 2015−2022.
(48) Boase, N. R. B.; Blakey, I.; Thurecht, K. J. Molecular Imaging with Polymers. *Polym. Chem.* **2012**, *3*, 1384−1389.
(49) Tirotta, I.; Dichiarante, V.; Pigliacelli, C.; Cavallo, G.; Terraneo, G.; Bombelli, F. B.; Metrangolo, P.; Resnati, G. ^{19}F Magnetic Resonance Imaging (MRI): From Design of Materials to Clinical Applications. *Chem. Rev.* **2015**, *115*, 1106−1129.
(50) Aime, S.; Castelli, D. D.; Crich, S. G.; Gianolio, E.; Terreno, E. Pushing the Sensitivity Envelope of Lanthanide-based Magnetic Resonance Imaging (MRI) Contrast Agents for Molecular Imaging Applications. *Acc. Chem. Res.* **2009**, *42*, 822−831.
(51) Liu, G.; Song, X.; Chan, K. W. Y.; McMahon, M. T. Nuts and Bolts of Chemical Exchange Saturation Transfer MRI. *NMR Biomed.* **2013**, *26*, 810−828.
(52) Rajca, A.; Wang, Y.; Boska, M.; Paletta, J. T.; Olankitwanit, A.; Swanson, M. A.; Mitchell, D. G.; Eaton, S. S.; Eaton, G. R.; Rajca, S. Organic Radical Contrast Agents for Magnetic Resonance Imaging. *J. Am. Chem. Soc.* **2012**, *134*, 15724−15727.
(53) Rajca, A.; Wang, Y.; Boska, M.; Paletta, J. T.; Olankitwanit, A.; Swanson, M. A.; Mitchell, D. G.; Eaton, S. S.; Eaton, G. R.; Rajca, S. Correction to Organic Radical Contrast Agents for Magnetic Resonance Imaging. *J. Am. Chem. Soc.* **2014**, *136*, 3318−3318.

DOI: 10.1021/acscentsci.7b00253
ACS Cent. Sci. 2017, 3, 800−811

(54) Hyodo, F.; Soule, B. P.; Matsumoto, K.-I.; Matusmoto, S.; Cook, J. A.; Hyodo, E.; Sowers, A. L.; Krishna, M. C.; Mitchell, J. B. Assessment of Tissue Redox Status Using Metabolic Responsive Contrast Agents and Magnetic Resonance Imaging. *J. Pharm. Pharmacol.* **2008**, *60*, 1049−1060.
(55) Hyodo, F.; Chuang, K.-H.; Goloshevsky, A. G.; Sulima, A.; Griffiths, G. L.; Mitchell, J. B.; Koretsky, A. P.; Krishna, M. C. Brain Redox Imaging Using Blood-brain Barrier-permeable Nitroxide MRI Contrast Agent. *J. Cereb. Blood Flow Metab.* **2008**, *28*, 1165−1174.
(56) Brasch, R. C. Work in Progress: Methods of Contrast Enhancement for NMR Imaging and Potential Applications. A Subject Review. *Radiology* **1983**, *147*, 781−788.
(57) Brasch, R. C.; London, D. A.; Wesbey, G. E.; Tozer, T. N.; Nitecki, D. E.; Williams, R. D.; Doemeny, J.; Tuck, L. D.; Lallemand, D. P. Work in Progress: Nuclear Magnetic Resonance Study of a Paramagnetic Nitroxide Contrast Agent for Enhancement of Renal Structures in Experimental Animals. *Radiology* **1983**, *147*, 773−779.
(58) Matsumoto, K.-I.; Hyodo, F.; Matsumoto, A.; Koretsky, A. P.; Sowers, A. L.; Mitchell, J. B.; Krishna, M. C. High-resolution Mapping of Tumor Redox Status by Magnetic Resonance Imaging Using Nitroxides as Redox-sensitive Contrast Agents. *Clin. Cancer Res.* **2006**, *12*, 2455−2462.
(59) Hyodo, F.; Matsumoto, K.-I.; Matsumoto, A.; Mitchell, J. B.; Krishna, M. C. Probing the Intracellular Redox Status of Tumors with Magnetic Resonance Imaging and Redox-sensitive Contrast Agents. *Cancer Res.* **2006**, *66*, 9921−9928.
(60) Zhelev, Z.; Bakalova, R.; Aoki, I.; Lazarova, D.; Saga, T. Imaging of Superoxide Generation in the Dopaminergic Area of the Brain in Parkinson's Disease, Using Mito-TEMPO. *ACS Chem. Neurosci.* **2013**, *4*, 1439−1445.
(61) Davis, R. M.; Sowers, A. L.; Degraff, W.; Bernardo, M.; Thetford, A.; Krishna, M. C.; Mitchell, J. B. A Novel Nitroxide is an Effective Brain Redox Imaging Contrast Agent and *in vivo* Radioprotector. *Free Radical Biol. Med.* **2011**, *51*, 780−790.
(62) Zhelev, Z.; Bakalova, R.; Aoki, I.; Matsumoto, K.-I.; Gadjeva, V.; Anzai, K.; Kanno, I. Nitroxide Radicals for Labelling of Conventional Therapeutics and Noninvasive Magnetic Resonance Imaging of Their Permeability for Blood-brain Barrier: Relationship between Structure, Blood Clearance, and MRI Signal Dynamic in the Brain. *Mol. Pharmaceutics* **2009**, *6*, 504−512.
(63) Doane, T. L.; Burda, C. The Unique Role of Nanoparticles in Nanomedicine: Imaging, Drug Delivery and Therapy. *Chem. Soc. Rev.* **2012**, *41*, 2885−2911.
(64) Jokerst, J. V.; Gambhir, S. S. Molecular Imaging with Theranostic Nanoparticles. *Acc. Chem. Res.* **2011**, *44*, 1050−1060.
(65) Joralemon, M. J.; McRae, S.; Emrick, T. PEGylated Polymers for Medicine: from Conjugation to Self-assembled Systems. *Chem. Commun.* **2010**, *46*, 1377−1393.
(66) Torchilin, V. Tumor Delivery of Macromolecular Drugs Based on the EPR Effect. *Adv. Drug Delivery Rev.* **2011**, *63*, 131−135.
(67) Anraku, Y.; Kishimura, A.; Kobayashi, A.; Oba, M.; Kataoka, K. Size-controlled Long-circulating PICsome as a Ruler to Measure Critical Cut-off Disposition Size into Normal and Tumor Tissues. *Chem. Commun.* **2011**, *47*, 6054−6056.
(68) Cabral, H.; Matsumoto, Y.; Mizuno, K.; Chen, Q.; Murakami, M.; Kimura, M.; Terada, Y.; Kano, M. R.; Miyazono, K.; Uesaka, M.; Nishiyama, N.; Kataoka, K. Accumulation of Sub-100 nm Polymeric Micelles in Poorly Permeable Tumours Depends on Size. *Nat. Nanotechnol.* **2011**, *6*, 815−823.
(69) Jokerst, J. V.; Lobovkina, T.; Zare, R. N.; Gambhir, S. S. Nanoparticle PEGylation for Imaging and Therapy. *Nanomedicine* **2011**, *6*, 715−728.
(70) Elliott, K. A. Metabolism of brain tissue slices and suspensions from various mammals. *J. Neurophysiol.* **1948**, *11*, 473−484.
(71) Tolmasoff, J. M.; Ono, T.; Cutler, R. G. Superoxide dismutase: correlation with lifespan and specific metabolic rate in primate species. *Proc. Natl. Acad. Sci. U. S. A.* **1980**, *77*, 2777−2781.
(72) Zhelev, Z.; Bakalova, R.; Aoki, I.; Matsumoto, K.-I.; Gadjeva, V.; Anzai, K.; Kanno, I. Nitroxyl Radicals as Low Toxic Spin-labels for Non-invasive Magnetic Resonance Imaging of Blood-brain Barrier Permeability for Conventional Therapeutics. *Chem. Commun.* **2009**, 53−55.
(73) Samuni, Y.; Gamson, J.; Samuni, A.; Yamada, K.; Russo, A.; Krishna, M. C.; Mitchell, J. B. Factors Influencing Nitroxide Reduction and Cytotoxicity *in Vitro*. *Antioxid. Redox Signaling* **2004**, *6*, 587−595.
(74) Merbach, A. S.; Helm, L.; Toth, E. *The Chemistry of Contrast Agent in Medical Magnetic Resonance Imaging*, 2nd ed.; John Wiley & Sons: Chichester, 2013.
(75) Caravan, P. Protein-targeted Gadolinium-based Magnetic Resonance Imaging (MRI) Contrast Agents: Design and Mechanism of Action. *Acc. Chem. Res.* **2009**, *42*, 851−862.
(76) Winalski, C. S.; Shortkroff, S.; Mulkern, R. V.; Schneider, E.; Rosen, G. M. Magnetic Resonance Relaxivity of Dendrimer-linked Nitroxides. *Magn. Reson. Med.* **2002**, *48*, 965−972.
(77) Winalski, C. S.; Shortkroff, S.; Schneider, E.; Yoshioka, H.; Mulkern, R. V.; Rosen, G. M. Targeted Dendrimer-based Contrast Agents for Articular Cartilage Assessment by MR Imaging. *Osteoarthr. Cartil.* **2008**, *16*, 815−822.
(78) Francese, G.; Dunand, F. A.; Loosli, C.; Merbach, A. E.; Decurtins, S. Functionalization of PAMAM Dendrimers with Nitronyl Nitroxide Radicals as Models for the Outer-sphere Relaxation in Dentritic Potential MRI Contrast Agents. *Magn. Reson. Chem.* **2003**, *41*, 81−83.
(79) Paletta, J. T.; Pink, M.; Foley, B.; Rajca, S.; Rajca, A. Synthesis and Reduction Kinetics of Sterically Shielded Pyrrolidine Nitroxides. *Org. Lett.* **2012**, *14*, 5322−5325.
(80) Sowers, M. A.; McCombs, J. R.; Wang, Y.; Paletta, J. T.; Morton, S. W.; Dreaden, E. C.; Boska, M. D.; Ottaviani, M. F.; Hammond, P. T.; Rajca, A.; Johnson, J. A. Redox Responsive Branched Bottebrush Polymers for *In Vivo* MRI and Fluorescence Imaging. *Nat. Commun.* **2014**, *5*, 5460.
(81) Xia, Y.; Li, Y.; Burts, A. O.; Ottaviani, M. F.; Tirrell, D. A.; Johnson, J. A.; Turro, N. J.; Grubbs, R. H. EPR Study of Spin Labeled Brush Polymers in Organic Solvents. *J. Am. Chem. Soc.* **2011**, *133*, 19953−19959.
(82) Burts, A. O.; Li, Y.; Zhukhovitskiy, A. V.; Patel, P. R.; Grubbs, R. H.; Ottaviani, M. F.; Turro, N. J.; Johnson, J. A. Using EPR to Compare PEG-*branch*-nitroxide "Bivalent-brush Polymers" and Traditional PEG Bottle-brush Polymers: Branching Makes a Difference. *Macromolecules* **2012**, *45*, 8310−8318.
(83) Liu, J.; Burts, A. O.; Li, Y.; Zhukhovitskiy, A. V.; Ottaviani, M. F.; Turro, N. J.; Johnson, J. A. Brush-first" Method for the Parallel Synthesis of Photocleavable, Nitroxide-labeled poly(ethylene glycol) Star Polymers. *J. Am. Chem. Soc.* **2012**, *134*, 16337−16344.
(84) Gao, A. X.; Liao, L.; Johnson, J. A. Synthesis of Acid-labile PEG and PEG-doxorubicin-conjugate Nanoparticles via Brush-first ROMP. *ACS Macro Lett.* **2014**, *3*, 854−857.
(85) Liao, L.; Liu, J.; Dreaden, E. C.; Morton, S. W.; Shopsowitz, K. E.; Hammond, P. T.; Johnson, J. A. A Convergent Synthetic Platform for Single-nanoparticle Combination Cancer Therapy: Ratiometric Loading and Controlled Release of Cisplatin, Doxorubicin, and Camptothecin. *J. Am. Chem. Soc.* **2014**, *136*, 5896−5899.
(86) Barnes, J. C.; Bruno, P. M.; Nguyen, H. V.-T.; Liao, L.; Liu, J.; Hemann, M. T.; Johnson, J. A. Using an RNAi Signature Assay to Guide the Design of Three-drug Conjugated Nanoparticles with Validated Mechanisms, *in vivo* Efficacy, and Low Toxicity. *J. Am. Chem. Soc.* **2016**, *138*, 12494−12501.
(87) Liu, J.; Gao, A. X.; Johnson, J. A. Particles Without a Box: Brush-first Synthesis of Photodegradable PEG Star Polymers under Ambient Conditions. *J. Visualized Exp.* **2013**, *80*, e50874.
(88) Burts, A. O.; Liao, L.; Lu, Y. Y.; Tirrell, D. A.; Johnson, J. A. Brush-first and Click: Efficient Synthesis of Nanoparticles that Degrade and Release Doxorubicin in Response to Light. *Photochem. Photobiol.* **2014**, *90*, 380−385.
(89) Love, J. A.; Morgan, J. P.; Trnka, T. M.; Grubbs, R. H. A Practical and Highly Active Ruthenium-based Catalyst that Effects the Cross Metathesis of Acrylonitrile. *Angew. Chem., Int. Ed.* **2002**, *41*, 4035−4037.

DOI: 10.1021/acscentsci.7b00253
ACS Cent. Sci. 2017, 3, 800−811

(90) Budil, D. E.; Lee, S.; Saxena, S.; Freed, J. H. Nonlinear-least-square Analysis of Slow-motion EPR Spectra in One and Two Dimensions Using a Modified Levenberg-Marquardt-algorithm. *J. Magn. Reson., Ser. A* **1996**, *120*, 155−189.
(91) Na, H. B.; Lee, J. H.; An, K.; Park, Y. I.; Park, M.; Lee, I. S.; Nam, D.-H.; Kim, S. T.; Kim, S.-H.; Kim, S.-W.; et al. Development of a T1 Contrast Agent for Magnetic Resonance Imaging Using MnO Nanoparticles. *Angew. Chem., Int. Ed.* **2007**, *46*, 5397−5401.
(92) Detappe, A.; Kunjachan, S.; Sancey, L.; Motto-Ros, V.; Biancur, D.; Drane, P.; Guieze, R.; Makrigiorgos, G. M.; Tillement, O.; Langer, R.; et al. Advanced multimodal nanoparticles delay tumor progression with clinical radiation therapy. *J. Controlled Release* **2016**, *238*, 103−113.
(93) Sancey, L.; Kotb, S.; Truillet, C.; Appaix, F.; Marais, A.; Thomas, E.; van der Sanden, B.; Klein, J. P.; Laurent, B.; Cottier, M.; et al. Long-Term in Vivo Clearance of Gadolinium-Based AGuIX Nanoparticles and Their Biocompatibility after Systemic Injection. *ACS Nano* **2015**, *9*, 2477−2488.
(94) Wei, H.; Bruns, O. T.; Kaul, M. G.; Hansen, E. C.; Barch, M.; Wisniowska, A.; Chen, O.; Chen, Y.; Li, N.; Okada, S.; Cordero, J. M.; Heine, M.; Farrar, C. T.; Montana, D. M.; Adam, G.; Ittrich, H.; Jasanoff, A.; Nielsen, P.; Bawendi, M. G. Exceedingly Small Iron Oxide Nanoparticles as Positive MRI Contrast Agents. *Proc. Natl. Acad. Sci. U. S. A.* **2017**, *114*, 2325−2330.
(95) Li, Y.; Lei, X.; Jockusch, S.; Chen, J. Y.-C.; Frunzi, M.; Johnson, J. A.; Lawler, R. G.; Murata, Y.; Murata, M.; Komatsu, K.; Turro, N. J. A Magnetic Switch for Spin-catalyzed Interconversion of Nuclear Spin Isomers. *J. Am. Chem. Soc.* **2010**, *132*, 4042−4043.
(96) Li, Y.; Lei, X.; Lawler, R. G.; Murata, Y.; Komatsu, K.; Turro, N. J. Distance-dependent Paramagnet-enhanced Nuclear Spin Relaxation of $H_2@C_{60}$ Derivatives Covalently Linked to a Nitroxide Radical. *J. Phys. Chem. Lett.* **2010**, *1*, 2135−2138.
(97) Sartori, E.; Ruzzi, M.; Lawler, R. G.; Turro, N. J. Nitroxide Paramagnet-induced Para-ortho Conversion and Nuclear Spin Relaxation of H_2 in Organic Solvents. *J. Am. Chem. Soc.* **2008**, *130*, 12752−12756.
(98) Keana, J. F. W.; Pou, S.; Rosen, G. M. Nitroxides as Potential Contrast Enhancing Agent for MRI Application: Influence of Structure on the Rate of Reduction by Rat Hepatocytes, Whole Liver Homogenate, Subcellular Fractions, and Ascorbate. *Magn. Reson. Med.* **1987**, *5*, 525−536.
(99) Bobko, A. A.; Kirilyuk, I. A.; Grigor'ev, I. A.; Zweier, J. L.; Khramtsov, V. V. Reversible Reduction of Nitroxides to Hydroxylamines: Role for Ascorbate and Glutathione. *Free Radical Biol. Med.* **2007**, *42*, 404−412.
(100) Blinco, J. P.; Fairfull-Smith, K. E.; Morrow, B. J.; Bottle, S. E. Profluorescent Nitroxides as Sensitive Probes of Oxidative Change and Free Radical Reactions. *Aust. J. Chem.* **2011**, *64*, 373−389.
(101) Yang, Y.; Zhao, Q.; Feng, W.; Li, F. Luminescent Chemodosimeters for Bioimaging. *Chem. Rev.* **2013**, *113*, 192−270.
(102) Ahn, H.-Y.; Fairfull-Smith, K. E.; Morrow, B. J.; Lussini, V.; Kim, B.; Bondar, M. V.; Bottle, S. E.; Belfield, K. D. Two-photon Fluorescence Microscopy Imaging of Cellular Oxidative Stress Using Profluorescent Nitroxides. *J. Am. Chem. Soc.* **2012**, *134*, 4721−4730.
(103) Workman, P.; Aboagye, E. O.; Balkwill, F.; Balmain, A.; Bruder, G.; Chaplin, D. J.; Double, J. A.; Everitt, J.; Farningham, D. A. H.; Glennie, M. J.; Kelland, L. R.; Robinson, V.; Stratford, I. J.; Tozer, G. M.; Watson, S.; Wedge, S. R.; Eccles, S. A. Guidelines for the Welfare and Use of Animals in Cancer Research. *Br. J. Cancer* **2010**, *102*, 1555−1577.
(104) Chapman, K.; Sewell, F.; Allais, L.; Delongeas, J.-L.; Donald, E.; Festag, M.; Kervyn, S.; Ockert, D.; Nogues, V.; Palmer, H.; Popovic, M.; Roosen, W.; Schoenmakers, A.; Somers, K.; Stark, C.; Stei, P.; Robinson, S. A Global Pharmaceutical Company Initiative: an Evidence-based Approach to Define the Upper Limit of Body Weight Loss in Short Term Toxicity Studies. *Regul. Toxicol. Pharmacol.* **2013**, *67*, 27−38.
(105) Rowland, M.; Benet, L. Z.; Graham, G. G. Clearance Concepts in Pharmacokinetics. *J. Pharmacokinet. Biopharm.* **1973**, *1*, 123−136.

DOI: 10.1021/acscentsci.7b00253
ACS Cent. Sci. 2017, 3, 800−811

Supporting Information for:

Nitroxide-Based Macromolecular Contrast Agents with Unprecedented Transverse Relaxivity and Stability for Magnetic Resonance Imaging of Tumors

Hung V.-T. Nguyen,[†] Qixian Chen,[†] Joseph T. Paletta,[‡] Peter Harvey,[∥] Yivan Jiang,[†] Hui Zhang,[‡] Michael D. Boska,[§] M. Francesca Ottaviani,[x] Alan Jasanoff,[∥,⊥,#] Andrzej Rajca,[‡] Jeremiah A. Johnson[†,*]

[†]*Department of Chemistry,* [∥]*Department of Biological Engineering,* [⊥]*Department of Brain and Cognitive Sciences, and* [#]*Department of Nuclear Science and Engineering, Massachusetts Institute of Technology, 77 Massachusetts Avenue, Cambridge, Massachusetts 02139, United States*

[§]*Department of Radiology, University of Nebraska Medical Center, Omaha, Nebraska 68198, United States*

[x]*Department of Pure and Applied Sciences, University of Urbino, Urbino 61029, Italy*

[‡]*Department of Chemistry, University of Nebraska, Lincoln, Nebraska 68588, United States*

*Email: jaj2109@mit.edu

Table of Contents

Section A. Materials / General Methods / Instrumentation

All reagents were purchased from commercial suppliers and used without further purification unless stated otherwise. Grubbs 3rd generation bispyridyl initiator,[1] macromonomers (MMs) **chex-MM**,[2] **Cy-MM**,[2] **PEG-MM**[3] and cross-linker **Acetal-XL**[3] were prepared according to literature procedures. Size exclusion chromatography (SEC) analyses were performed on an Agilent 1260 Infinity setup with two Shodex KD-806M columns in tandem and a 0.025 M LiBr DMF mobile phase run at 60 °C. The differential refractive index (dRI) of each compound was monitored using a Wyatt Optilab T-rEX detector, and the light scattering (LS) signal was acquired with a Wyatt Dawn Heleos-II detector. Column chromatography was carried out on silica gel 60F (EMD Millipore, 0.040–0.063 mm).

Dynamic light scattering (DLS) measurements were performed using a Wyatt Technology Mobius DLS instrument. Samples were prepared at 1.0 mg/mL in either nanopure water (MilliQ), PBS buffer, or 5% glucose solution (in nanopure water). The resulting solutions were passed through a 0.4 μm Nalgene filter (PES membrane) into disposable polystyrene cuvettes, which were pre-cleaned with compressed air. Measurements were made in sets of 10 acquisitions, and the average hydrodynamic diameters were calculated using the DLS correlation function via a regularization fitting method (Dynamics 7.4.0.72 software package from Wyatt Technology).

TEM images were acquired using a FEI Tecnai Multipurpose TEM (G2 Spirit TWIN, 12kV) at the MIT Center for Materials Science and Engineering. Samples were prepared as follows: 5 μL of a 1.0 mg/mL aqueous solution of BASP-ORCA was pipetted onto a carbon film-coated 200-mesh copper grid (Electron Microscopy Sciences) placed on a piece of parafilm. Next, the solution was carefully absorbed at the base of the droplet using the edge of a Kimwipe, leaving behind the nanoparticles on the TEM grid. The samples were then negatively stained by adding a drop of 2 wt% uranyl acetate (Electronic Microscopy Sciences). After 3 min, the residual uranyl acetate solution was carefully absorbed onto a Kimwipe, and the samples were allowed to dry completely.

Excitation/emission spectra and fluorescence measurements were acquired using a Tecan Infinite® 200 Pro plate reader. Electron Paramagnetic Resonance (EPR) spectra were acquired at the University of Nebraska using a Bruker CW X-band spectrometer equipped with a frequency counter. The spectra were obtained using a dual mode cavity; all spectra were recorded using an oscillating magnetic field perpendicular (TE_{102}) to the swept magnetic field. DPPH powder (g = 2.0037) was used as a g-value reference.

Relaxivity measurements by MRI: Phantom MRI data were acquired in a 12 cm outer diameter birdcage transceiver for imaging in a 20 cm bore Bruker 7 T Avance III MRI scanner. Samples at varying concentrations (0 up to 5 mM) in PBS buffer were loaded into the wells of a 384-well clear polystyrene plate (Thermo Scientific Nunc), which had been pre-cut in half to optimally fit the coil. Unused wells were filled with PBS buffer. 2 mm slices were imaged through the samples with the field of view of 5 x 5 cm and the data matrices were 256 x 256 points. Longitudinal (r_1)

and transverse (r_2) relaxivity measurements were acquired using multi-spin multi-echo (MSME) sequences (flip angle = 180°). r_1; TE = 12 ms, TR = 300, 350, 400, 450, 500, 600, 800, 1000, 1200, 1500, 3000, 5000, 10000 ms. r_2; TR = 5000 ms, TE = 12, 24, 36, 48, 60, 72, 84, 96, 108, 120, 132, 144, 156, 168, 280, 192, 204, 216, 228, 240, 252, 264, 276, 288, 300, 312, 324, 336, 348, 360 ms. Custom routines written in Matlab (Mathworks, Natick, MA) were used to reconstruct the images and compute relaxation time constants by fitting image intensity data to exponential decay curves.

Kinetics of nitroxide quenching by EPR spectroscopy: A solution was prepared with ascorbic acid (Asc), sodium phosphates (<30 ppm transition metals), sodium hydroxide and diethylenetriaminepentaacetic acid (DTPA, ~0.1% (mol/mol) to sodium phosphates) at pH 7.4. Reduced L-GSH was then dissolved to provide the Asc/GSH solution. BASP-ORCA solution was prepared in phosphate buffer, which was made from sodium phosphates and DTPA (~0.1% (mol/mol) to sodium phosphates) at pH 7.4. Equal volumes of the freshly prepared 1 mM (in nitroxide) sample solution and 20 mM Asc/GSH solution were combined and vortexed for 6 seconds, and then added to a 2 mm OD EPR tube. Kinetic studies were performed on 0.5 mM nitroxide solution in the presence of 125 mM sodium phosphates, 10 mM Asc, and 10 mM GSH. The peak height of the low-field line of the triplet was measured as a function of time. Microwave power was kept under 6.5 mW and the temperature was controlled at 295 K with a nitrogen flow system.

Computational analysis of nitroxide quenching by EPR spectroscopy: The EPR spectra are constituted by a "fast" and a "slow" component. From visual inspection, it was clear that the slow component was changing from one to another sample, while the fast one showed an almost equivalent line shape in the three spectra. Therefore, we first tried a computation (program by Budil and Freed[4]) of the fast component to be subtracted from the three spectra to obtain a reliable line shape for the slow components. We succeeded with the fast component shown in Figure S3A (see Section C for Figure S3A-C) (the subtracted experimental line in black and the computed line is in red). The main parameters used for the computation are shown in the figure and described below. Subtraction of this fast component from the overall spectra produced the three slow components shown in Figures S3B, S3C and S3D for 1 min, 40 min, and 180 min, respectively (in Figures S3A-S3D the spectra are normalized in height). Their computations are shown as well, together with the main parameters used for computation and analysis. The following parameters were calculated

• The g_{ii} components for the coupling between the electron spin and the magnetic field (accuracy from computation ± 0.0002). The starting values, which were used in previous studies[5] using nitroxide radicals, are 2.009, 2.006, 2.003, for g_{xx}, g_{yy}, and g_{zz}, respectively. We found that these values worked for the computations of the fast component and for the t = 1 min slow component; however, for computing the slow components of t = 40 min and 180 min it was necessary to decrease the g_{zz} values to 2.0025 and 2.002, respectively. This observation indicated an increased structural anisotropy of the nitroxide labels from 1 min to 40 min to 180 min.

• The A_{ii} components for the coupling between the electron spin and the nitroxide-nitrogen nuclear spin (accuracy from computation ± 0.5 G). These parameters increase with an increase in the environmental polarity of the nitroxide. Mainly, as done in previous studies,[5] the A_{xx} and A_{yy} values were maintained constant (6 G) and only A_{zz} was changed. The polarity was found to be slightly lower for the fast component (A_{zz} = 35 G) than for the slow one (A_{zz} = 36 G); it was constant for the different slow components.

• The correlation time for rotational diffusion of the radical, τ (accuracy from computation ± 0.05 ns). This parameter increases with an increase in the local viscosity around the nitroxide group and with a decrease in the rotational mobility of the nitroxide. The local viscosity largely increased (the mobility decreased) from the fast component to the slow ones and it also increased (the mobility decreased) from 1 min (10 ns) to 40 min (11 ns) to 180 min (13.2 ns). Notably, by performing a subtraction procedure using the double integrals of the components of the spectra, it was found that the fast component was contained in all the three spectra in almost the same relative percentage, that is, about 20 % (the accuracy in this percentage is about 1 %).

• The line width (accuracy from computation ± 0.1 G), which measures spin-spin interactions due to a high local concentration of paramagnetic species (like colliding nitroxide groups in fast motion, or nitroxides bound in close proximity in slow motion). The line width was quite high for all samples, indicating a high local concentration of nitroxides, but it was the highest (7.6 G) for the slow component of the *t* = 1 min sample, and it decreased at 40 min (5.5 G) and further decreased at 180 min (4.2 G). The latter value is even smaller than the line width of the fast component (4.8 G).

Fluorimetry: Fluorescence analysis was performed using a Tecan Infinite® 200 Pro plate reader. Absorption/emission spectra of **BASP-ORCA1** were acquired to determine $\lambda_{ex/em}$, which were 640 nm and 705 nm respectively (as expected for the dye used in these studies: Cyanine5.5). Absorption spectra were acquired using a 1 nm wavelength step size at 9 nm bandwidth; emission spectra were obtained using λ_{ex} of 640 nm, a 5 nm wavelength step size, and 10 nm bandwidth. To examine the effect of nitroxide-quenching on fluorescence emission intensity, samples were prepared in 96-well plates (Corning, *n* = 3) by mixing 50 µL of 5 mg **BASP-ORCA1**/mL solution with 50 µL of Asc/GSH solution with one of the following compositions: 120 equivalences (eq, with respect to **chex**) Asc, 60 eq Asc, 40 eq Asc, and 60 eq Asc + 60 eq GSH. Control samples (*n* = 3) were prepared by mixing 50 µL of 5 mg **BASP-ORCA1**/mL solution with 50 µL of PBS. Fluorescence intensity was monitored continuously for 2 h; a plateau was typically reached within 40-50 min.

Cell culture: A549 and HeLa cells (ATCC) were cultured in DMEM media (Sigma-Aldrich) supplemented with 10% fetal bovine serum (FBS, VWR) and 1% penicillin/streptomycin (Thermo Fisher Scientific). Human umbilical vein endothelial cells (HUVEC, Lonza) were cultured in EGM^+ media (Lonza) supplemented with 1% penicillin/streptomycin. All cells were housed in 5% CO_2 humidified atmosphere at 37 °C.

In vitro cell viability: HUVEC cells were plated at 5,000 cells per well (in 100 µL) in 96-well collagen-coated plates (Corning) and allowed to adhere overnight. The media was then replaced with fresh media containing **BASP-ORCA1** at various concentrations. The plate was incubated for 72 h, and cell viability was then determined using the CellTiter-Glo assay (Promega). HeLa cells were plated in 96-well plates (Corning) and cytotoxicity was studied following the same experimental procedure used for HUVEC cells.

Animal usage: All experiments involving animals were reviewed and approved by the MIT Committee for Animal Care (CAC). BALB/c mice (female, 8-12 weeks old, Taconic) were used for *in vivo* toxicity, pharmacokinetic studies, and biodistribution (n = 3). NCR-NU nude mice (female, 8-12 weeks old, Taconic) were used for *in vivo* MRI, NIRF imaging, and biodistribution (n = 3). All animals received an alfalfa-free diet (TestDiet) at least 2 weeks prior to the start of the studies to minimize auto-fluorescence.

In vivo toxicity: Solutions containing 5.0–30 mg of **BASP-ORCA1** in 5% glucose were prepared, passed through sterile 0.2 µm filter (Nalgene, PES membrane), and administered into BALB/c mice via tail vein injection. The mice were monitored over a period of 30 d. Initial injections were performed in one mouse for each dose, all of which appeared to be well-tolerated. The highest dose (30 mg) was then administered to another set of mice (n = 3). No adverse physical effects and/or significant weight losses were observed.

In vivo MR and NIRF imaging instrumentation: All imaging experiments were performed at the Koch Institute for Integrative Cancer Research at MIT. *In vivo* MRI was acquired using a Varian 7T/310/ASR-whole mouse MRI system. Scans were collected with respiratory gating (PC-SAM version 6.26 by SA Instruments Inc.) to avoid confounding noise due to chest movement. The respiratory rate and animal temperature were closely monitored during image collection. Coronal T_2 weighted images (T_2WIs) were collected using the fast spin echo multiple slices pulse sequence with T_R=4000 ms; $T_{E(eff)}$=48 ms; ETL=8; FOV=100×50 mm^2; 512×256 matrix and 2 averages over 12 slices of 1 mm thickness and 0 mm gap. Axial T2WIs were collected using the fast spin echo multiple slices pulse sequence with T_R=4000 ms; $T_{E(eff)}$=48 ms; ETL=8; FOV=45×45 mm^2; 256×256 matrix and 2 averages over 10-16 (to capture entire tumor) slices of 1 mm thickness and 0 mm gap.

In vivo NIRF imaging was performed on an IVIS Spectrum-bioluminescent and fluorescent imaging system (Xenogen). Epi-fluorescence imaging was acquired through excitation of the Cy5.5 fluorophore ($\lambda_{ex}/\lambda_{em}$ = 640/700 nm, exposure time 2-10s) present in **BASP-ORCA1**.

Pharmacokinetics (PK) and biodistribution (BD) studies: **BASP-ORCA1** doses (5.0 mg in 5% glucose) were prepared, passed through sterile 0.2 µm filters, and injected into BALB/c mice (groups of n = 3). Blood samples were taken at 1, 3, 6, 24, and 48h via cardiac puncture after euthanization in a CO_2 chamber. The blood samples were subjected to fluorescence imaging (IVIS, Cy5.5 $\lambda_{ex}/\lambda_{em}$ = 640/700 nm, Xenogen) for analysis of blood-compartment PK. For BD, organs

from these BALB/c mice were harvested and subjected to fluorescence imaging (IVIS, Cy5.5 $\lambda_{ex}/\lambda_{em}$ = 640/700 nm, Xenogen).

In vivo MR and NIRF imaging in tumor-bearing mice: A549 cells were cultured in DMEM media supplemented with 10% fetal bovine serum and 1% penicillin/streptomycin in 5% CO_2 humidified atmosphere (37 °C) to a final concentration of 20%. Cells were then harvested, mixed with Matrigel and sterile pH 7.4 PBS buffer (1:1), filtered through sterile 0.2 μm filters, and injected subcutaneously (2.0 x 10^6 cells) into the hind flank of NCR-NU mice. Tumor growth was monitored for 2–4 weeks until appropriate cumulative diameters (~ 1 cm) were achieved.

MRI and NIRF images were acquired for each animal (n = 3-4) before injections. **BASP-ORCA1** doses (0.16 mmol **chex**/kg or 0.23 mmol **chex**/kg in 5% glucose) were prepared, passed through a sterile 0.2 μm filter, and administered to the tumor-bearing mice via tail vein injection. Tumor imaging was done at pre-determined time points; at the last imaging time point, mice were immediately euthanized in a CO_2 chamber, and organs were collected, imaged by NIRF, and stored in dry ice for EPR analysis.

Ex vivo EPR spectroscopy: Harvested organs were shipped on dry ice to the University of Nebraska, where they were stored on dry ice. For EPR sample preparation, each tissue sample, one at a time, was rapidly thawed and transferred to a weighed vial; 900 μL of PBS buffer (0.5 mM, pH 7.2) was then added. The mixture was put into an ice-water bath and homogenized with a rotor stator homogenizer, then pipetted into a 4-mm outer diameter EPR sample tube. The samples were degassed by sonication as needed (for instance, when gas bubbles were visible). The EPR tube was capped, sealed with parafilm, and stored briefly in acetone/dry ice bath before spin concentration measurements.

Spin concentrations of nitroxide radicals in tissues (μmol **chex** per g protein; *Note:* see below for details of protein content determination) were measured at −30 °C (243.2 K) to increase signal-to-noise of the aqueous samples. Measurements of tissue samples were alternated with that of the spin concentration reference (see next paragraph) and g-value reference (2,2-diphenyl-1-picrylhydrazyl powder was used as the g-value reference). For tissue samples with low signal-to-noise, the cavity background was recorded with identical parameters, including number of scans and receiver gain. Typical parameters were as follows: microwave attenuation—20 dB, modulation amplitude—5 Gauss, spectral width—300 Gauss, resolution—512 points, conversion—40.96, time constant—10.24, and sweep time—20.97 s. These parameters were kept identical for the tissues, references, and cavity backgrounds. The number of scans (8–256) and receiver gain were adjusted as needed for each sample.

The reference for spin concentration was 0.50 mM Proxyl in PBS (pH 7.2). This reference was always stored in dry ice, except during measurements, and occasionally re-checked for spin concentration decay.

Protein content determination: The protein content of tissue homogenate samples was determined using the BCA Protein Assay Kit (ThermoFisher Scientific). These protein contents were then used as a normalizing parameter to compare nitroxide spin concentration and NIRF signal (Figure 6b, main text).

Ex vivo NIRF Imaging: To acquire BD, the collected organs and organ homogenates were subjected to NIRF imaging following the same aforementioned experimental procedure as for *in vivo* NIRF imaging. Furthermore, tissue homogenate samples were transferred into a 96-well plate and imaged for the correlation of NIRF signal and spin concentration.

In vivo MRI data analysis: Signal intensities pre- and post- injection were compared only using slices where tumors and muscle were clearly visible. Using ImageJ software, a region of interest (ROI) around each component was manually drawn. The average signal intensity and area of the ROI were measured; these data were then normalized against the signal intensity of the muscle tissue. Signal intensity was acquired by multiplying area and normalized signal intensity. This process was repeated for all relevant slices for a given organ; the sum of these signal intensities was then calculated and divided for the total area, affording the volume-averaged signal intensity. Signal enhancement by **BASP-ORCA1** was quantified by comparing the volume-averaged signal intensities pre- and post-injection.

Statistical analysis: nanoparticle diameter acquired by DLS and TEM, as well as ascorbate quenching kinetics of **BASP-ORCA1** by EPR results were reported as average ± standard deviation. *In vitro* and *in vivo* studies of **BASP-ORCA1** results were reported as mean ± standard error of the mean. Statistical comparisons were determined using student t-test where applicable.

Section B. Procedure for BASP-ORCA Synthesis

Note: *All BASP-ORCA syntheses were performed in a glovebox under N_2 atmosphere; however, similar results are expected under ambient conditions. All ROMP reactions followed the same general procedure, which was modified from literature examples.*[3,6]

*Representative procedure for BASP-ORCA synthesis with brush length of 7.07 (m) and 20 equivalents (N) of cross-linker (**BASP-ORCA1, m = 7.07, N = 20**):* To a 4 mL vial, a suspension of **Acetal-XL** (15.6 mg, 26.8 µmol, 20.0 eq) in THF (268.0 µL, 0.1 M **Acetal-XL**) was prepared. To a second 4 mL vial containing a stir bar, **chex-MM** (35.0 mg, 9.4 µmol, 7.0 eq) was added; **Cy-MM** was then added from a premade 12.5 mg/mL solution in THF (30.6 µL, 0.094 µmol, 0.07 eq). To a third vial, a solution of Grubbs 3rd generation bispyridyl catalyst (Grubbs III, 0.02 M in THF) was freshly prepared. THF (91.8 µL) was then added to the **MM** vial, followed by the addition of Grubbs III solution (67.0 µL, 1.3 µmol, 1.0 eq) to give the desired **MM**:Grubbs III ratio of 7.07:1 (1 mol % of the **Cy-MM**), while achieving a total **MM** concentration of **0.05 M**, affording a dark blue solution. The reaction mixture was allowed to stir for 30 min at room temperature before an aliquot (~5 µL) was taken out and quenched with 1 drop of ethyl vinyl ether for GPC analysis. The **Acetal-XL** suspension was then added dropwise (in aliquots of 5 eq, or ~70 µL, every 5 minutes) over the course of 20 min into the **MM** vial, and the polymerizing mixture was allowed to stir for 6 h at room temperature, affording a dark blue solution. To quench the polymerization, a drop of ethyl vinyl ether was added. The reaction mixture was transferred to an 8 kD molecular weight cutoff dialysis tubing (Spectrum Laboratories) in 10 mL nanopure water, and the solution was dialyzed against water (500 mL X 3, solvent exchange every 6 h). The solution of BASP-ORCA was then lyophilized to afford a blue solid.

Other BASP compositions were prepared as follows: **MM**:Grubbs III ratios of 9.99:1, 7.07:1, or 5.05:1 (*m* values). **Acetal-XL** were used in 15, 20, or 30 equivalences (*N* values). PEG-BASP, which contained no **chex**-MM, was prepared in an analogous manner to BASP-ORCAs using a PEG-MM lacking **chex**.[3] **Chex**-bottlebrush was prepared as previously described.[2]

Section C. Supplementary Figures Cited in the Main Text

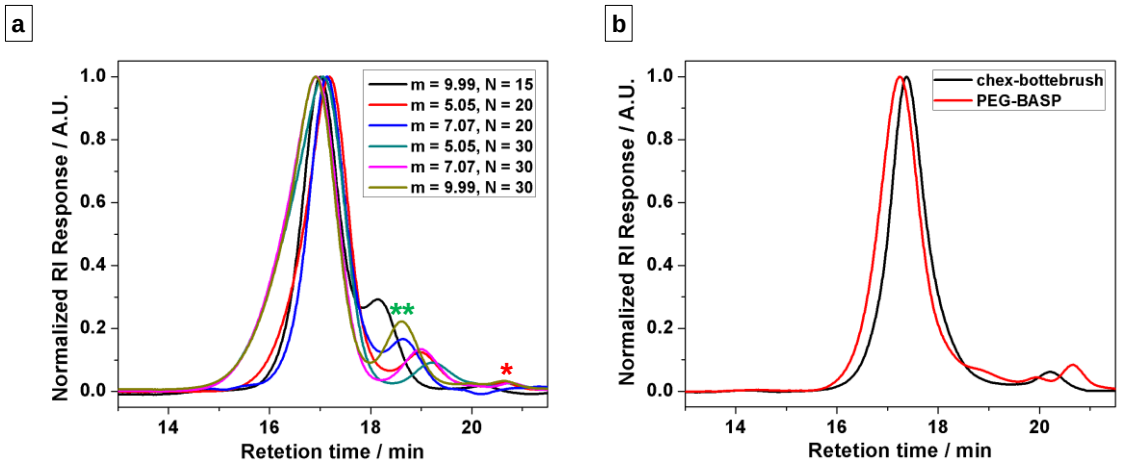

Figure S1. a. GPC traces of BASP-ORCAs with different brush length (*m*) and cross-linker equivalents (*N*). ***indicates** negligible residual MM; ****denotes** uncoupled bottlebrush. In all cases, the MM-to-bottlebrush conversions were almost quantitative, while the bottlebrush-to-BASP conversions were ≥ 85%. **b.** GPC traces of **chex**-bottlebrush and PEG-BASP used for phantom MRI comparison with **BASP-ORCA1**.

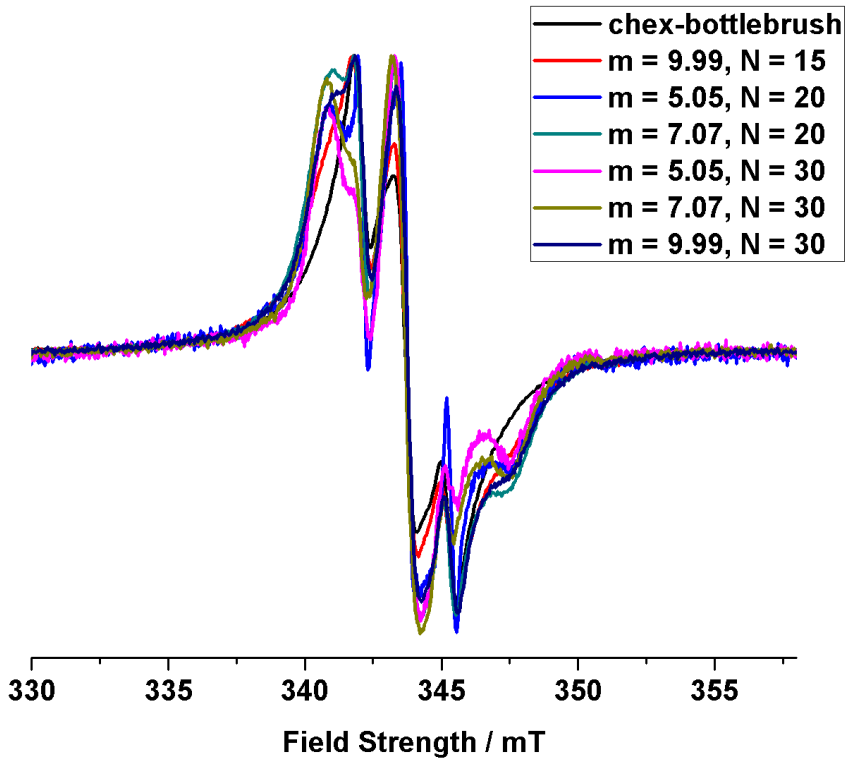

Figure S2. EPR spectra for BASP-ORCAs of varying composition.

Nitroxide Reduction Kinetics:

Table S1. Kinetics of the reduction of nitroxides with 20-fold molar excess of ascorbate (Asc) and 0-25-fold molar excess of glutathione (GSH). Numerical fits to pseudo-first order rate equation (*k'*) peak height (PH) or integrated peak height (IPH) of the low-field EPR line.

							Initial Kinetics (<1 h)					Late Kinetics (>1 h)			
Compd	Run No.	Run Label	Data used	Nitrox Conc. (mM)	Asc. Conc. (mM)	GSH Conc. (mM)	Range of fits	k' × 10^4 (s^{-1})	R^2	k × 10^4 ($M^{-1}s^{-1}$)	Avg k × 10^4 ($M^{-1}s^{-1}$)	Range of fit (h)	k' × 10^4 (s^{-1})	R^2	k × 10^4 ($M^{-1}s^{-1}$)
BASP-ORCA1[a]	1	JP1191	IPH	0.5	10	10	<1000	3.294	0.8795	329.4	366 ± 25	1.2-2.8	0.672	0.9923	67.2
			IPH*[a]					3.40	0.9948	339.7	334 ± 55		0.586	0.9994	58.6
			PH					0.836	0.8721	83.6			0.297	0.9943	29.7
	2	JP1190	IPH	0.5	10	10	115-595	3.712	0.7664	371.2					
			IPH*[a]					3.408	0.9910	340.8					
			PH					3.377	0.2923	33.77					
	3	JP1189	IPH	0.5	10	10	113-613	3.828	0.7646	382.8					
			IPH*[a]					3.238	0.9863	323.7					
			PH					5.07	0.3068	50.7					
	4	JP1188	IPH	0.5	10	10	126-603	3.818	0.5387	381.8					
			IPH*[a]					3.311	0.9938	331.1					
			PH					5.072	0.3366	50.72					
	1	YW982	IPH	0.5	10	5.0	177–897	3.27	0.9633	327.0	306[b]				
chex-bottlebrush			PH					3.42	0.9702	342.0	308[b]				
	2	YW983	IPH	0.5	10	5.0	396–1019	2.85	0.9520	285.0		1.1-2.8	0.416	0.9216	41.6
			PH					2.73	0.9895	273.0			0.386	0.9938	38.6
	1	YW981	IPH	0.5	10	0.0	251–851	3.05	0.9439	305.0	296[b]				
chex-bottlebrush			PH					2.41	0.9808	241.0	254[b]				
	2	YW985	IPH	0.5	10	0.0	278–878	2.86	0.9145	286.0		1.3-2.8	0.243	0.8838	24.3
			PH					2.68	0.9775	268.0			0.196	0.9735	19.6
chex-dendrimer[7]	1	JP609	IPH	0.5	10	0.0	90-390	6.20	0.6609	620.0	603 ± 123	0.8-2.8	0.301	0.6847	30.1
			PH					6.17	0.9718	617.0	579 ± 59.6		0.354	0.9663	35.4
	2	JP610	IPH	0.5	10	0.0	115-415	7.18	0.6743	718.0					
			PH					6.09	0.9336	609.0					
	3	JP611	IPH	0.5	10	0.0	126-426	4.72	0.7984	472.0					
			PH					5.10	0.9915	510.0					
3-CP[8]	1	JP899	IPH	0.2	4.0	5.0	<600	2.435	0.9997	608.8	608.0 ± 4.2				
			PH					2.361	0.9990	590.3	602.6 ± 25				
	2	JP8100	IPH	0.2	4.0	5.0	<600	2.438	0.9997	609.6					
			PH					2.410	0.9996	602.4					
	3	JP1101	IPH	0.2	4.0	5.0	<600	2.423	0.9998	605.6					
			PH					2.461	0.9996	615.2					
3-CP[7,9]	1	JP460	IPH	0.2	4.0	0.0	<3600	2.547	0.9996	636.8	625 ± 22				
			PH					2.504	0.9949	636.0	611 ± 44				
	2	JP461	IPH	0.2	4.0	0.0	<3600	2.498	0.9975	624.5					
			PH					2.396	0.9949	599.0					
	3	JP462	IPH	0.2	4.0	0.0	<3600	2.459	0.9999	614.8					
			PH					2.389	0.9961	597.3		>1	1.18	0.9952	295

[a] For **BASP-ORCA1**, double integration of entire EPR spectra gave initial rate constant k = 449 ± 23 $M^{-1}s^{-1}$, which is somewhat larger than the integrated peak height (IPH) value, k = 366 ± 25 $M^{-1}s^{-1}$; IPH* is the integrated peak height for the center line of the EPR spectrum. [b] For ORCA-Fluor, initial second order rate constants from 4 kinetic runs using 0 – 10 equiv of GSH, k = 301 ± 20 and 281 ± 43 $M^{-1}s^{-1}$ for baseline corrected IPH and PH data. Data for **chex**-bottlebrush,[2] data for **chex**-dendrimer (baseline corrected) and late kinetics for **3-CP** with Asc only,[7] data for **3-CP** with 20 equiv of Asc and 25 equiv of GSH,[8] and data for **3-CP** with Asc only[9] were reported elsewhere); the reported values represent the mean and standard deviation (*n = 2-4*).

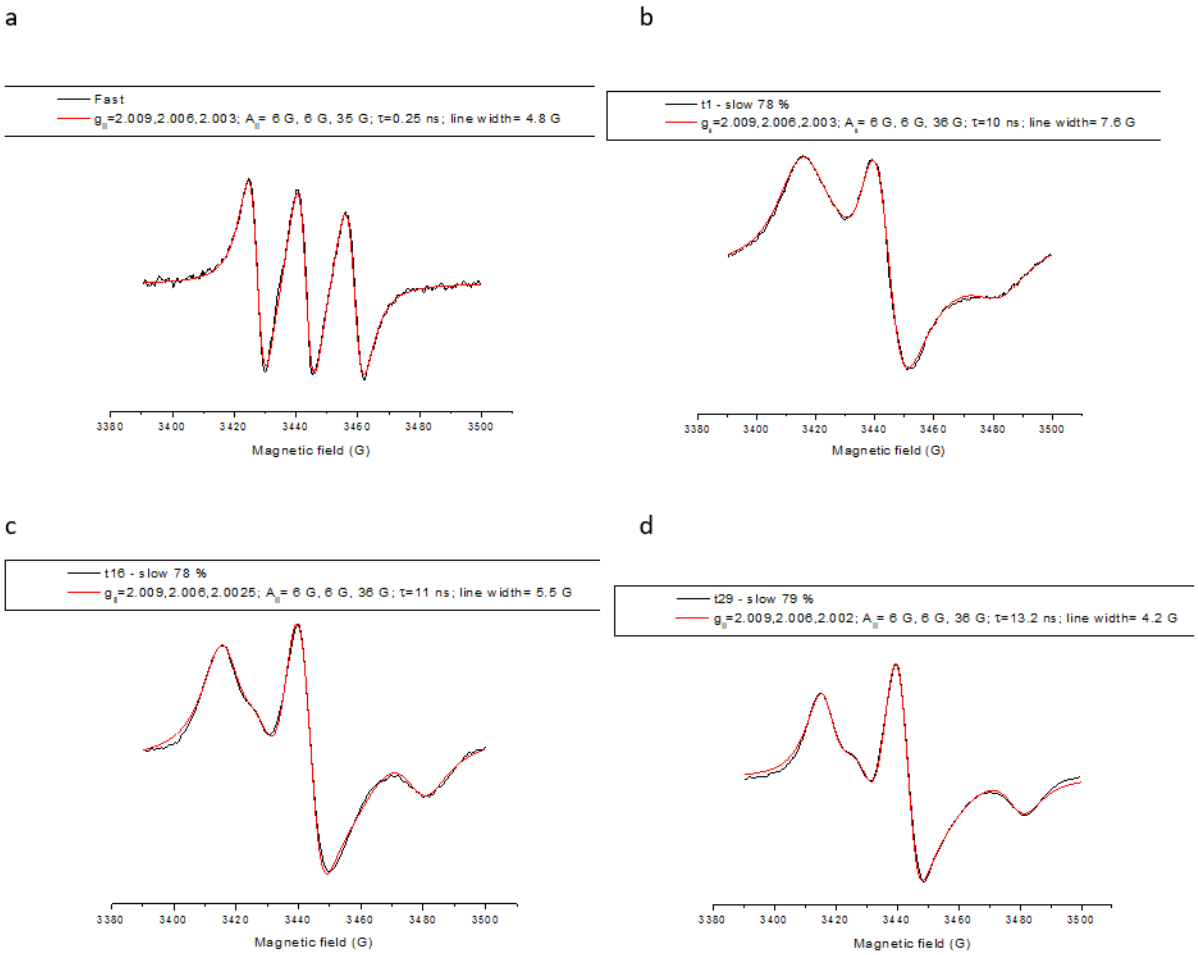

Figure S3. Computational analysis of EPR spectra obtained during reduction kinetics experiments: **a.** fast component **b.** t1 = 1 min **c.** t16 = 40 min and **d.** t29 = 180 min of slow component following addition of Asc solution.

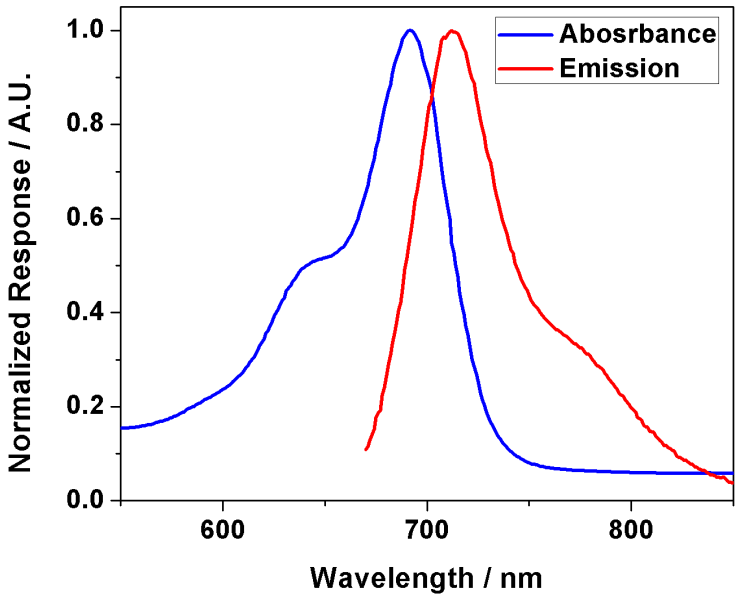

Figure S4. Excitation and emission spectra of **BASP-ORCA1**.

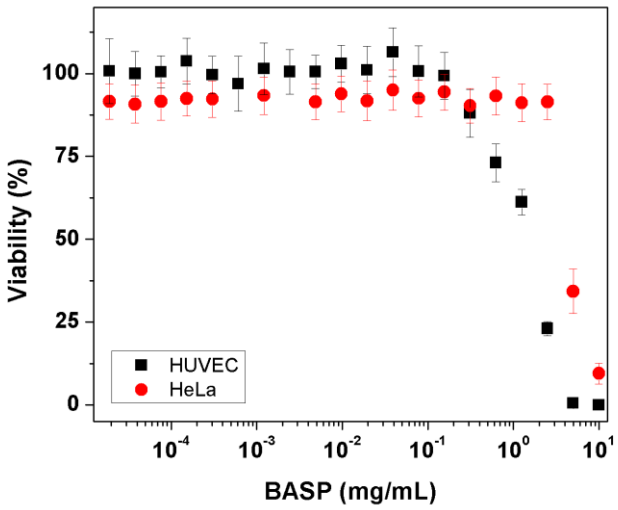

Figure S5. Cell viability assay for **BASP-ORCA1** in the toxin-sensitive HUVEC and cancerous HeLa cell lines as measured by CellTiter Glo. No toxicity was observed until high concentrations were reached (up to 0.3 mg/mL and 5 mg/mL for HUVEC and HeLa, respectively); the reported values represent the mean and standard error of the mean (*n* = *4*).

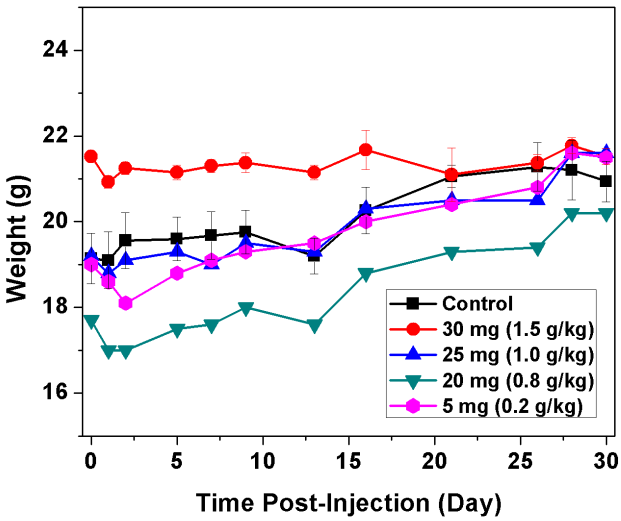

Figure S6. *In vivo* gross toxicity of **BASP-ORCA1** following intravenous injections in BALB/c mice; the reported values represent the mean and standard error of the mean. The control and highest dose experiments were performed with n = 3, whereas lower doses were done with n = 1.

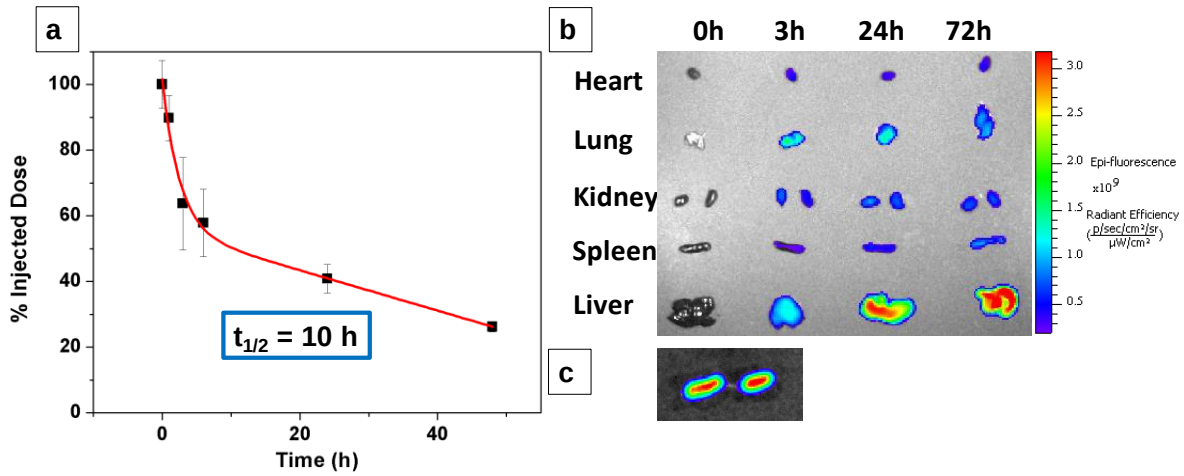

Figure S7. **a.** Pharmacokinetics (PK), **b.** biodistribution (BD), and **c.** excrements collected 24 h after administration of **BASP-ORCA1** in BALB/c mice as imaged by NIRF ($\lambda_{ex}/\lambda_{em}$ = 640/700 nm). PK data were fit into a two-component model using standard procedures (R^2 = 0.95).[2,5] The reported values represent the mean and standard error of the mean (*n* = *3*).

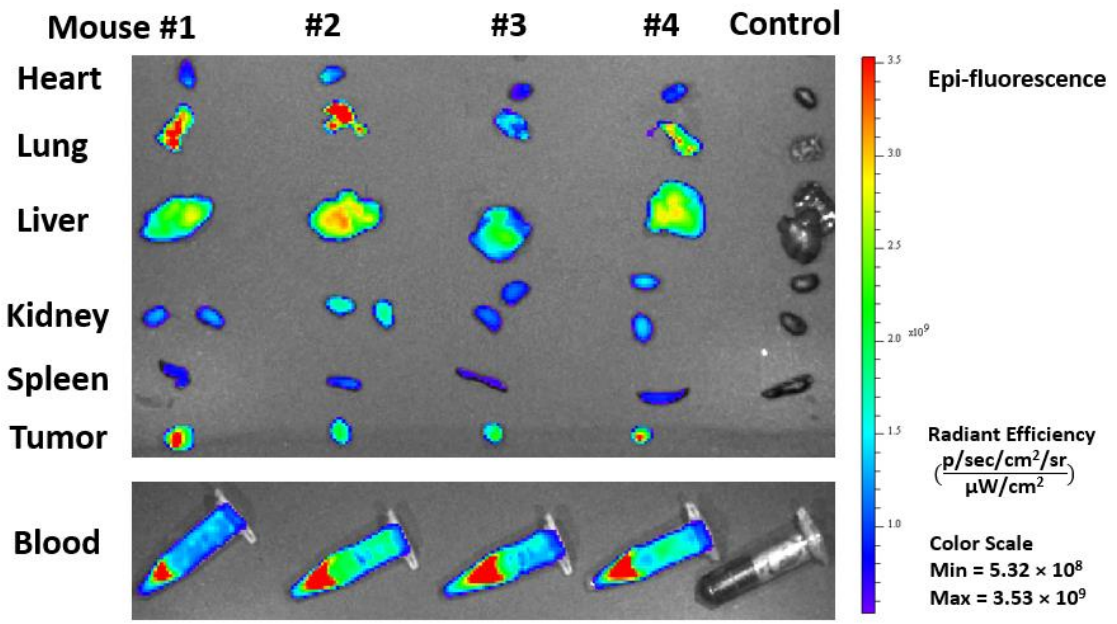

Figure S8. *Ex vivo* BD as assessed by NIRF imaging ($\lambda_{ex}/\lambda_{em}$ = 640/700 nm) of subcutaneous tumor-bearing NCR-NU mice following injection of **BASP-ORCA1**. Experiments were done with n = 4.

Section D. References

1 Love, J. A.; Morgan, J. P.; Trnka, T. M.; Grubbs, R. H. A Practical and Highly Active Ruthenium-based Catalyst that Effects the Cross Metathesis of Acrylonitrile. *Angew. Chem. Int. Ed.* **2002**, *41*, 4035–4037.

2 Sowers, M. A.; McCombs, J. R.; Wang, Y.; Paletta, J. T.; Morton, S. W.; Dreaden, E. C.; Boska, M. D.; Ottaviani, M. F.; Hammond, P. T.; Rajca, A.; Johnson, J. A. Redox-Responsive Branched-bottlebrush Polymers for *in vivo* MRI and Fluorescence Imaging. *Nat. Commun*. **2014**, *5*, 5460.

3 Gao, A. X.; Liao, L.; Johnson, J. A. Synthesis of Acid-Labile PEG and PEG-doxorubicin-conjugate Nanoparticles via Brush-first ROMP. *ACS Macro Lett*. **2014**, *3,* 854–857.

4 Budil, D. E.; Lee, S.; Saxena, S.; Freed, J. H. Nonlinear-least-square Analysis of Slow-motion EPR Spectra in One and Two Dimensions Using a Modified Levenberg-Marquardt-algorithm. *J. Magn. Reson., Ser. A*. **1996**, *120*, 155-189

5 Angelov, V.; Velichkova, H.; Ivanov, E.; Kotsilkova, R.; Delville, M-H.; Cangiotti, M.; Fattori, A.; Ottaviani, M. F. EPR and Rheological Study of Hybrid Interfaces in Gold-clay-epoxy Nanocomposites. *Langmuir.* **2014**, *30*, 13411-13421.

6 Liao, L.; Liu, J.; Dreaden, E. C.; Morton, S. W.; Shopsowitz, K. E.; Hammond, P. T.; Johnson, J. A. A Convergent Synthetic Platform for Single-nanoparticle Combination Cancer Therapy: Ratiometric Loading and Controlled Release of Cisplatin, Doxorubicin, and Camptothecin. *J. Am. Chem. Soc*. **2014**, *136*, 5896–5899.

7 Rajca, A.; Wang, Y.; Boska, M.; Paletta, J. T.; Olankitwanit, A.; Swanson, M. A.; Mitchell, D. G.; Eaton, S. S.; Eaton, G. R.; Rajca, S. Organic Radical Contrast Agents for Magnetic Resonance Imaging. *J. Am. Chem. Soc.* **2012**, *134*, 15724-15727.

8 Wang, Y.; Paletta, J. T.; Berg, K.; Reinhart, E.; Rajca, S.; Rajca, A. Synthesis of Unnatural Amino Acids Functionalized with Sterically Shielded Pyrroline Nitroxides. *Org. Lett.* **2014**, *16*, 5298–5300.

9 Paletta, J. T.; Pink, M.; Foley, B.; Rajca, S.; Rajca, A. Synthesis and Reduction Kinetics of Sterically Shielded Pyrrolidine Nitroxides. *Org. Lett.* **2012**, *14*, 5322-5325.